Environmental Science and Pollution Research (2024) 31:9764–9783
https://doi.org/10.1007/s11356-023-31796-8

RESEARCH ARTICLE

Magnetically separable $Co_{0.6}Fe_{2.4}O_4$/MIL-101-NH_2 adsorbent for Congo red efficient removal

Zhenhong Zhang[1] · Yuye Zhong[1] · Peng Sun[2] · Pingping Zhao[1] · Houbin Li[1] · Xinghai Liu[3]

Received: 22 October 2023 / Accepted: 27 December 2023 / Published online: 9 January 2024

Abstract

The development of effective and practical adsorbents for eliminating pollutants still remains a significant challenge. Herein, we synthesized a novel magnetically separable composite, $Co_{0.6}Fe_{2.4}O_4$/MIL-101-NH_2, through the in-situ growth of MIL-101-NH_2 on magnetic nanoparticles, designed specifically for the removal of Congo red (CR) from aqueous solutions. MIL-101-NH_2 possessed high BET surface area (240.485 $m^2•g^{-1}$) and facile magnetic separation function and can be swiftly separated (within 30 s) through an external magnetic field post-adsorption. The investigation systematically explored the influence of crucial parameters, including adsorbent dosage, pH, adsorption duration, temperature, and the presence of interfering ions, on CR adsorption performance. Findings indicate that CR adsorption adheres to the pseudo-second-order (PSO) kinetic model and the Langmuir isotherm model. Thermodynamic analysis reveals the spontaneity, endothermic nature, and orderly progression of the adsorption process. Remarkably, the adsorbent with 0.1 $g•L^{-1}$ boasts an impressive maximum adsorption capacity of 1756.19 $mg•g^{-1}$ for CR at 298.15 K, establishing its competitive advantage. The reuse of the adsorbent over 5 cycles remains 78% of the initial adsorption. The CR adsorption mechanisms were elucidated, emphasizing the roles of π-π interactions, electrostatic forces, hydrogen bonding, and metal coordination. Comparison with other dyes, such as methylene blue (MB) and methyl orange (MO), and exploration of adsorption performance in binary dye systems, demonstrates the superior capacity and selectivity of this adsorbent for CR. In conclusion, our magnetically separable metal–organic framework (MOF)based composite presents a versatile and effective solution for CR removal, with promising applications in water treatment and environmental remediation.

Keywords Adsorption · Congo red · $Co_{0.6}Fe_{2.4}O_4$ · Magnetic MOF · MIL-101-NH_2

Introduction

With the relentless march of modernization and industrialization, there has been a staggering surge in the release of untreated organic pollutants into wastewater. This alarming trend has exacerbated the water scarcity crisis and posed grave threats to both human well-being and ecological stability. Shockingly, reports indicate that a staggering 200,000 tons of dyes is annually released into the global environment without undergoing any treatment (Marnani and Shahbazi 2019). In China alone, a staggering 160 million cubic meters of dye wastewater is discharged into our aquatic ecosystems every year (Islam and Mostafa 2018). Organic dyes, as a category of highly hazardous pollutants frequently found in wastewater, with contact toxicity, latent pathogenicity, and carcinogenic potential, and through cumulative effects can have a significant impact on ecosystems (Khan et al. 2022; Sarkodie et al. 2023). Furthermore, the presence of

---

Responsible Editor: Tito Roberto Cadaval Jr

Zhenhong Zhang and Yuye Zhong contributed equally to this work.

Highlights

- The magnetic adsorbent with embedded structure is compounded by in-situ growth.
- The Langmuir isotherm shows the high adsorption capacity of $Co_{0.6}Fe_{2.4}O_4$/MIL-101-NH_2 for Congo red (up to 1756.19 $mg•g^{-1}$) at 298.15 K.
- The excellent separability and reusability of the adsorbent show its practicability and industrialization feasibility.
- $Co_{0.6}Fe_{2.4}O_4$/MIL-101-NH_2 has strong adsorption performance in complicated environments due to its selectivity for Congo red.

Extended author information available on the last page of the article

chromophores or chromophore-like elements such as nitro ($-NO_2$), azo (–N = N-), primary amine ($-RNH_2$), and triarylmethane in dye molecules enables them to absorb light to varying degrees (Brown 1981; Christovam et al. 2022). This not only diminishes the aesthetic appeal of water bodies but also hampers the development of aquatic organisms. One such dye of concern is CR, a bis-azo dye commonly employed in industries like printing, dyeing, textiles, and paper manufacturing (Adebayo et al. 2022). CR is likewise both toxic and resistant to degradation, necessitating rigorous treatment of its industrial wastewater to meet environmental discharge standards.

To date, various wastewater treatment technologies, including biodegradation, chemical precipitation, photocatalytic degradation, and coagulation, have made significant strides in development (Abujazar et al 2022; Selvaraj et al. 2021). Nonetheless, these methods exhibit certain drawbacks, including their intricate and cumbersome procedures, substantial energy consumption, and elevated costs. In stark contrast, the conventional adsorption offers distinct advantages. Leveraging the porous structure of adsorbents and their strong affinity for target molecules, it facilitates the separation of pollutants, thereby circumventing the aforementioned limitations (Ghazvini et al. 2021). Although traditional adsorbents like activated carbon (Benmaamar et al. 2019), bentonite (Jiang et al 2022), zeolite (Imessaoudene et al. 2023), and resin (Xu et al. 2020) have been applied for dye removal in wastewater, they typically exhibit limited capacity and specificity. In pursuit of more efficient adsorbents, researchers have turned their attention toward emerging porous materials.

MOFs are fashioned through the bonding of metal ions or metal clusters with organic chains, held together by weak coordination bonds (Jeong et al. 2023; Mazloomi et al. 2019). MOFs are prized for their diverse structures, flexibility in adjustment, outstanding pore structures, generous specific surface areas, and ease of surface functionalization (Esrafili et al. 2022; Huang et al. 2023; Shi et al. 2023). MIL-101-NH_2(Fe), in particular, stands out as a strong contender due to its utilization of the non-toxic transition metal Fe, which offers an abundance of adsorption active sites. Its expansive specific surface area and open cavities enhance site accessibility, rendering it exceptional in the realm of pollutant removal (Lian et al. 2019). It is noteworthy that the activity of amidogen ($-NH_2$) MOF and the positioning of modification sites can introduce additional diffusion interactions between the ligand and the skeleton (Lim et al. 2022; Liu et al. 2022a; Pallach et al. 2021; Razavi et al. 2022). This subsequently impacts the energy landscape and pore structure of the MIL-101-NH_2, ultimately altering its adsorption capabilities for the better. Whereas MOF's remarkable water dispersibility and powder form pose a significant challenge in recyclability, leading to a substantial increase in the cost of adsorption and creating a bottleneck in its practical application. The introduction of magnetic components, especially Fe3O4, is regarded as an important means to solve such difficulty (Mahmoudian et al. 2023; You et al. 2018; Zheng et al. 2023). The complementary and compatible nature of Fe_3O_4 and MOF has paved the way for their widespread integration into composite structures (Cheng et al. 2023; He et al. 2023; Lee et al. 2023; Li et al. 2020; Lu et al. 2022; Wang et al. 2021b; Zheng et al. 2018). Nevertheless, it is essential to acknowledge that the magnetism of Fe_3O_4 is easily weakened by oxidation and lose their effectiveness, but the addition of another magnetic substance, like Co, Mn, and Ni, can create a binary magnetic oxide, bolstering its chemical stability and enhancing mass transfer efficiency (Cross et al. 2023; Wang et al. 2021a, 2019).

The novelty of this study is centered around the first-time synthesis and application of $Co_{0.6}Fe_{2.4}O_4$/MIL-101-NH_2 for dye industry wastewater treatment, with a particular focus on the removal of CR. A series of characterizations were conducted to attest the successful preparation of $Co_{0.6}Fe_{2.4}O_4$/MIL-101-NH_2. The study showed satisfactory results in the adsorption capacity, specific selectivity, and reusability of $Co_{0.6}Fe_{2.4}O_4$/MIL-101-NH_2 for the removal of azo dye CR. These reveal that the $Co_{0.6}Fe_{2.4}O_4$/MIL-101-NH_2 can provide a viable option for the removal of other organic dyes or similar compounds from wastewater. Therefore, the research objectives in this study are summarized as follows: preparing $Co_{0.6}Fe_{2.4}O_4$/MIL-101-NH_2 adsorbent and its characterization, exploring the effects of a series of factors on CR adsorption, systematically studying the isotherm, kinetics, and thermodynamics characteristics of adsorption of $Co_{0.6}Fe_{2.4}O_4$/MIL-101-NH_2 to CR, exploring the repeated use and specific selectivity of $Co_{0.6}Fe_{2.4}O_4$/MIL-101-NH_2, and clarifying the adsorption mechanism.

Materials and methods

Chemical and materials

$FeCl_3 \bullet 6H_2O$ were acquired from Shanghai McLean Biochemical Technology Co., Ltd. (Shanghai, China). Cobalt chloride hexahydrate ($CoCl_2 \bullet 6H_2O$), ferrous sulfate heptahydrate ($FeSO_4 \bullet 7H_2O$), oxalic acid dihydrate ($H_2C_2O_4 \bullet 2H_2O$), ethylene glycol (EG), N, N-dimethylformamide (DMF), polyvinylpyrrolidone (PVP, K-30), and ethanol absolute (EtOH) were supplied by Sinopharm Chemical Reagent Co., Ltd. (Shanghai, China). 2-Aminoterephthalic acid (NH_2-TPA), aerosol OT (AOT), and CR were purchased from Shanghai Aladdin Biochemical Technology Co., Ltd. (Shanghai, China). All reagents were of analytical grade and used without further treatment. Deionized water (DI) was adopted to all aqueous solution.

Instrumentations

The Fourier transform infrared (FT-IR) spectral was recorded on a Thermo Scientific Nicolet 5700 (America) with KBr pellets in the 4000–500 cm^{-1} region. Powder X-ray diffraction (PXRD) patterns were acquired by Rigaku Mini Flex 600 (Japan) diffractometer at 40 kV among 3.0–80.0 (2*θ*) with V-filtered Cr Ka radiation. The size and morphology of materials were observed on a Zeiss Gemini SEM 500 (Germany) field emission scanning electron microscope (FESEM) equipped with an Oxford Ultim Max 65 (Britain) energy dispersive X-ray spectroscope (EDS). The thermal gravimetric analysis (TGA) curves were obtained by a NETZSCH TG209 F1 Libra (Germany) thermogravimetric analyzer. The test was carried out in the nitrogen environment and with a 20 mL•min^{-1} rate (room temperature–800 °C, 10 °C•min^{-1}). The BET test was determined by Micromeritics 3FLEX (America) through N_2 adsorption. Magnetic properties of the samples were characterized by the Lake Shore 7404 (America) vibrating sample magnetometer (VSM) among ± 2 T at room temperature. The zeta potential of samples was measured by a Malvern Zerasizer 3690 (Britain) zeta potential analyzer. The Fe leaching experiment was tested by PQ-MS (Germany) inductively coupled plasma mass spectrometry (ICP-MS). Characterization of the elements contained in the samples was caught by an Thermo Fisher Scientific Escalab250Xi (America) X-ray spectrometer (XPS).

Synthesis of $Co_{0.6}Fe_{2.4}O_4$

Magnetic nanoparticles ($Co_{0.6}Fe_{2.4}O_4$) were prepared by conventional co-precipitation method (Zeng et al. 2014), as Fig. 1 a. Firstly, AOT (1.78 g) was dissolved in a mixture of EG (20 mL) and DI (20 mL) to make a homogeneous solution, and two identical above solutions were prepared and denoted as liquid A and liquid B, respectively. Subsequently, $CoCl_2$•$6H_2O$ (0.19 g) and $FeSO_4$•$7H_2O$ (0.89 g) were added to liquid A, and oxalic acid (0.50 g) was dispersed to liquid B. Immediately after mixing liquid A with liquid B and stirring the mixed solution at 25 °C for 6 h, the reaction was washed with EtOH and DI three times, and the orange precipitate was collected by centrifugation and dried under vacuum at 50 °C for 12 h. Finally, the obtained light yellowish powder was heated in a tube furnace at 1 ℃•min^{-1} to 400 °C for 2 h to obtain black magnetic $Co_{0.6}Fe_{2.4}O_4$ particles.

Preparation of MIL-101-NH_2

MIL-101-NH_2 was synthesized using solvothermal method as reported previously. NH_2-TPA (0.23 g) was firstly dissolved in DMF (10 mL). Simultaneously, $FeCl_3$•$6H_2O$ (0.68 g) was scattered in another DMF (10 mL). The two DMF solutions were mixed into a Teflon-lined stainless steel autoclave and reacted in an oven at 110 °C for 20 h. After cooling, the precipitate was washed with DMF and

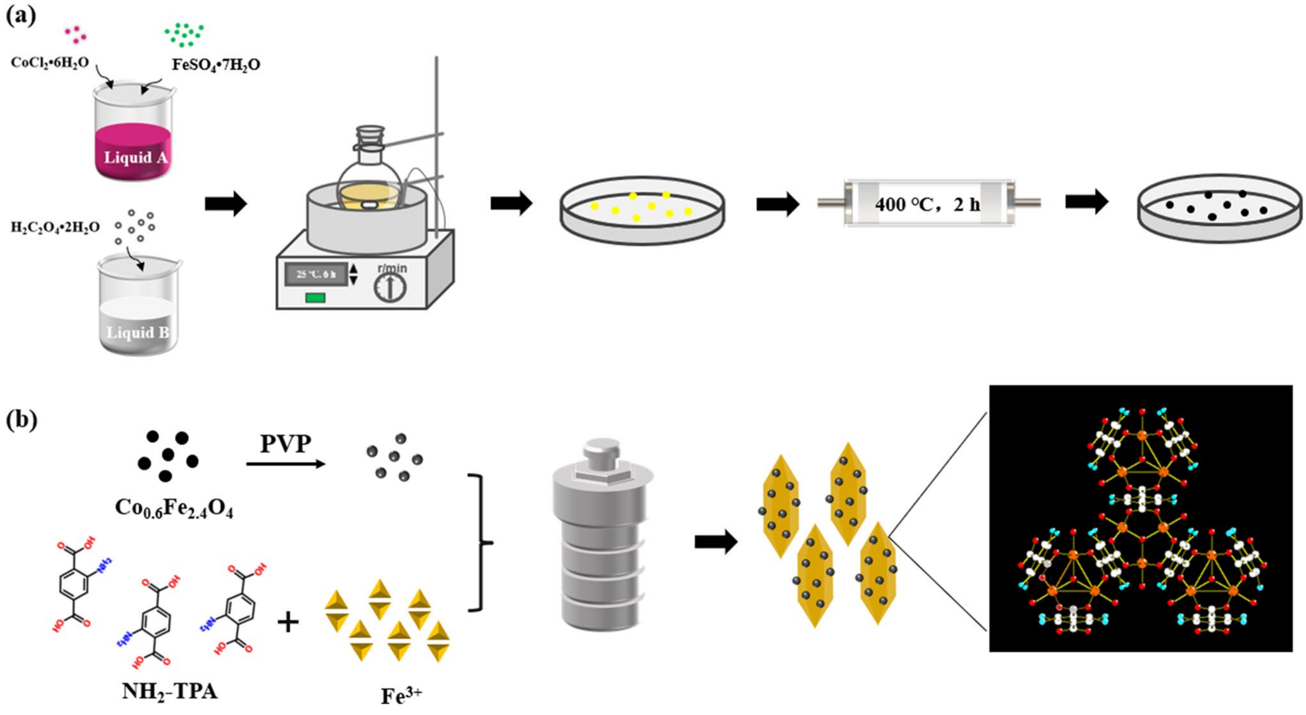

Fig. 1 Schematic diagram of preparation for $Co_{0.6}Fe_{2.4}O_4$ (**a**) and $Co_{0.6}Fe_{2.4}O_4$/MIL-101-NH_2 (**b**)

EtOH several times, centrifuged, and dried to obtain brown MIL-101-NH_2.

Preparation of $Co_{0.6}Fe_{2.4}O_4$/MIL-101-NH_2

As seen in Fig. 1 b, the surfactant PVP (0.40 g) was firstly dissolved in DMF (10 mL), then magnetic nanoparticles (0.17 g) needed to be appended to the aforesaid DMF solution and sonicated for 1 h at room temperature before the addition of quantitative NH_2-TPA. The following procedure was the same as the preparation of MIL-101-NH_2.

Batch adsorption experiment

Batch adsorption experiments were carried out under continuous mechanical stirring at a speed of 300 rpm and protected from light. Three replicate experiments were performed and the average values were taken to reduce the error. The effects of adsorbent dosage, time, CR concentrations, pH, and interfering ions were analyzed by measuring the removal of CR by the adsorbents. After adsorption, the solution was filtered through a 0.45-μm microporous membrane and the concentration of CR in the filtrate was measured using ultraviolet (UV-3600) at the maximum absorption wavelength ($\lambda_{max}=497$ nm). The pH of the CR solution was adjusted adopting 0.1 M HCl or NaOH solution. The removal rate (r, %) and adsorption capacity (Q_t, mg•g^{-1}) were calculated by Eqs. (1) and (2).

$$r = \frac{C_t - C_0}{C_0} * 100\% \tag{1}$$

$$Q_t = \frac{\left(C_0 - C_t\right) * V}{m} \tag{2}$$

where C_0 (mg•L^{-1}) and C_t (mg•L^{-1}) are the initial and final concentrations of CR before and after certain adsorption time, mg•L^{-1}; V (L) is the volume of CR solution; m (g) is the mass of adsorbent.

Results and discussion

Characterization

Figure 2 a shows the XRD spectra of $Co_{0.6}Fe_{2.4}O_4$, MIL-101-NH_2, and $Co_{0.6}Fe_{2.4}O_4$/MIL-101-NH_2. The formation of magnetic cobalt-iron bimetallic oxides with good crystallinity is demonstrated by the diffraction peaks of 2θ at 18.44° (1 1 1), 30.34° (2 2 0), 35.66° (3 1 1), 37.26° (2 2 2), 43.28° (4 0 0), 53.64° (4 2 2), 57.26° (5 1 1), 62.82° (4 4 0), 65.86° (5 3 1), 71.14° (6 2 0), 74.28° (5 3 3), 75.44° (6 2 2), and 79.24° (4 4 4). These peaks agree with the typical spinel $CoFe_2O_4$ (JCPDS No. 22–1086). Based on prior reports in the literature (Li et al. 2017; Song et al. 2021), the high crystallinity diffraction peaks of MIL-101-NH_2 (Fe) correspond with the distinctive diffraction peaks situated at $2\theta = 9.36°$, 10.26°, 16.68°, 18.72°, and 20.65°. The effective fabrication of the composite $Co_{0.6}Fe_{2.4}O_4$/MIL-101-NH_2 is justified by the synchronized emergence of the distinctive peaks of both components on the XRD spectrum of magnetic MOF.

The functional groups of the prepared materials were qualitatively analyzed by FT-IR spectroscopy (Fig. 2 b). For $Co_{0.6}Fe_{2.4}O_4$, the broad peaks near 595 cm^{-1} and 1635 cm^{-1} are related to the stretching vibration of Fe–O, Co–O, and C = O bond (Olusegun and Mohallem 2020). The peaks of Fe–O and Co–O of $Co_{0.6}Fe_{2.4}O_4$/MIL-101-NH_2 are red-shifted (to 617 cm^{-1}), which indicates that the two components are successfully compounded. In the spectrogram of MIL-101-NH_2, the peak near 1492 cm^{-1} belongs to the vibrational mode of C = C in the benzene ring, the peaks at 1617 cm^{-1} and 769 cm^{-1} are connected with the in-plane and out-of-plane bending vibration of N–H bond, the wavenumbers of 1337 cm^{-1} and 1258 c^{--1} are corresponding to the stretching vibration of C–N bond, and the peaks observed at 1581 cm^{-1} and 1431 cm^{-1} are the results of the antisymmetric and symmetric stretching vibrations of COO–, respectively (Zhang et al. 2020). The two distinctive COO– peaks experience a blue shift as the outcome of the compositing procedure. The O–H stretching vibration associated with the large peak around 3417 cm^{-1} is mostly due to the water that the sample has absorbed.

Raman spectra of the three materials were recorded and compared to demonstrate the material structure changes when MIL-101-NH_2 was combined with magnetic particles (Fig. 2 c). In MIL-101-NH_2, sharp peaks around 1768, 1442, 1426, 1260, 801, and 685 cm^{-1} are indicative of the distinctive metal terephthalate vibrations (Song et al. 2021). The 688 and 479 cm^{-1} in $Co_{0.6}Fe_{2.4}O_4$ agree with the characteristic vibrations of Co–O and Fe–O, respectively (Zhao et al. 2017). Characteristic peaks of two components emerged in $Co_{0.6}Fe_{2.4}O_4$/ MIL-101-NH_2 and some of them shift to a certain extent, implying that the components had successfully undergone recombination.

As indicated in the literature (Zeng et al. 2014), the chemical formulation of the precursor for the magnetic oxide can be represented as $Co_{0.2}Fe_{0.8}C_2O_4$•$2H_2O$. The composition of the magnetic oxide was substantiated through TGA analysis of the precursor. As delineated in Fig. 2 d, prior to attaining a temperature of 400 °C, the precursor undergoes two distinct stages of mass reduction, registering at 20.12% and 39.17%, respectively. These correspond to two distinct processes: the release of crystalline water and the carbonization of $Co_{0.2}Fe_{0.8}C_2O_4$•$2H_2O$. It is from these measurements that we can deduce the chemical formula of the resultant magnetic material to be $Co_{0.6}Fe_{2.4}O_4$. It is noteworthy that the

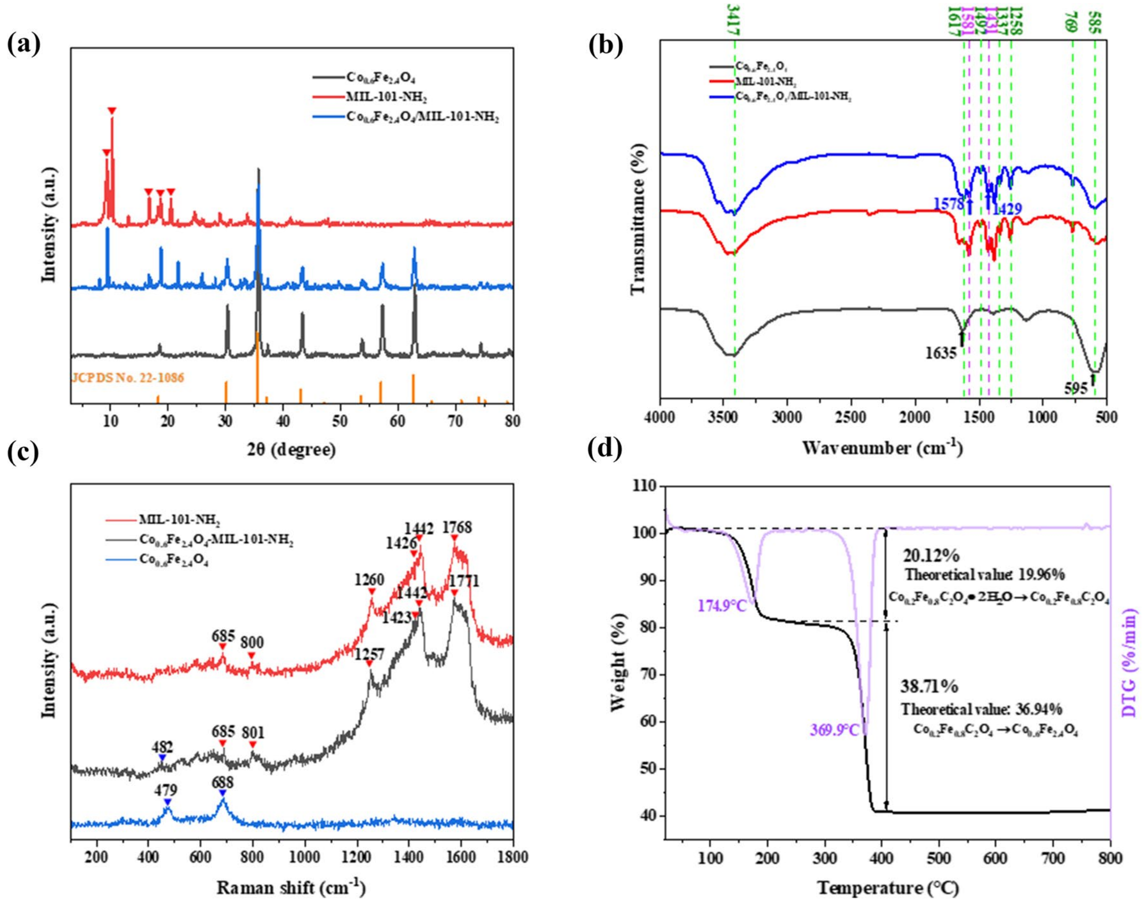

Fig. 2 XRD images (**a**), FT-IR images (**b**), and Raman patterns (**c**) of $Co_{0.6}Fe_{2.4}O_4$, MIL-101-NH_2, and $Co_{0.6}Fe_{2.4}O_4$/MIL-101-NH_2; TG and DTG (**d**) curves of the precursor of magnetic oxide

weight loss rate in the second stage exhibits some deviation from the theoretical value, potentially attributed to the volatilization of residual solvent molecules (Zeng et al. 2014).

The microstructure and particle size of the materials were meticulously examined via SEM. It is readily apparent that the synthesized $Co_{0.6}Fe_{2.4}O_4$ exhibited stick-like particle morphology, as illustrated in Fig. 3 a. The MOF particles displayed a distinctive octahedral structure, characterized by a uniform surface and particle size, as depicted in Fig. 3 b. These findings align harmoniously with previously report (Song et al. 2021). It is clear from a thorough look of the magnetic MOF's SEM pictures (Fig. 3 c, d) that the spindle-like surface was scattered with large numbers of granular nanoparticles. The cause of this particular morphology may be that certain magnetic particles encapsulated within the MIL-101-NH_2 shell affected the crystalline nucleation of MOF. Consequently, the $Co_{0.6}Fe_{2.4}O_4$/MIL-101-NH_2 takes on a spindle-shaped polyhedral form and is a roughly five-fold enlargement in sizes (width: 664.86 nm; length: 2153.13 nm). The solvothermal process also wielded an impact on the microscopic structure and size of $Co_{0.6}Fe_{2.4}O_4$, leading to the conversion of magnetic particles, i.e., from previous stick shape to substantial nanoparticles dispersed on the MOF's surface. Figure 3 e–k provides a comprehensive view of the EDS images of the magnetic MOF. By scrutinizing the distribution of three key elements—N, Fe, and Cothe morphological transformations of $Co_{0.6}Fe_{2.4}O_4$ and MIL-101-NH_2 within the magnetic MOF, along with the distribution of $Co_{0.6}Fe_{2.4}O_4$ within the MOF shell and on its surface, were further affirmed. All of these results clearly show that $Co_{0.6}Fe_{2.4}O_4$/MIL-101-NH_2 is not only a physical mixing of $Co_{0.6}Fe_{2.4}O_4$ and MIL-101-NH_2 distribution diagram that the pore sizes of them are mostly distributed between 2 and 10 nm (MIL-101-NH_2 and $Co_{0.6}Fe_{2.4}O_4$/MIL-101-NH_2) and 5 and 20 nm ($Co_{0.6}Fe_{2.4}O_4$), further confirming the mesoporous structure of the sample. The BET specific surface areas of MIL-101-NH_2, $Co_{0.6}Fe_{2.4}O_4$, and $Co_{0.6}Fe_{2.4}O_4$/MIL-101-NH_2 are 142.159, 44.796, and 240.485 m^2•g^{-1}, respectively. The increase of specific surface area after recombination indicates that the porous structure of the composite components and the uniform dispersion of the components during the compounding

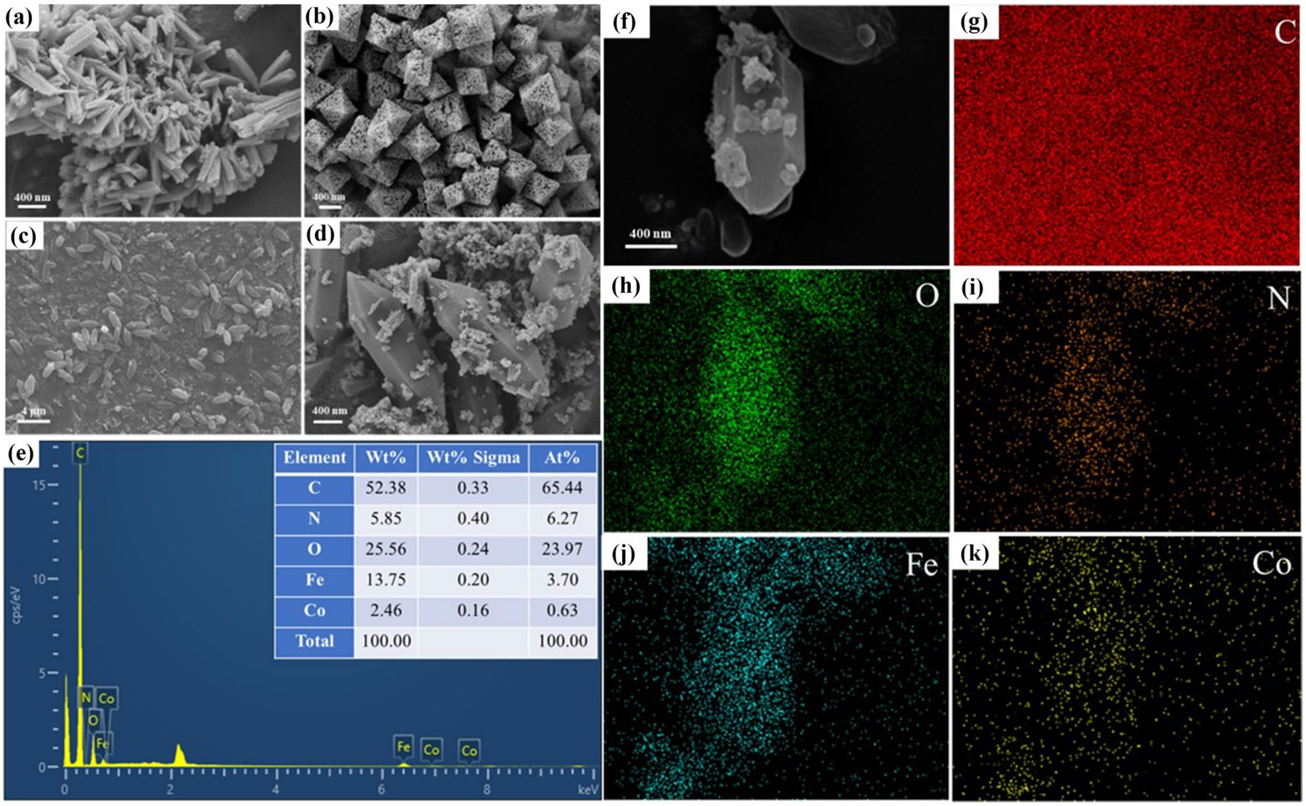

Element	Wt%	Wt% Sigma	At%
C	52.38	0.33	65.44
N	5.85	0.40	6.27
O	25.56	0.24	23.97
Fe	13.75	0.20	3.70
Co	2.46	0.16	0.63
Total	100.00		100.00

Fig. 3 SEM images of $Co_{0.6}Fe_{2.4}O_4$ (**a**), MIL-101-NH_2 (**b**), and $Co_{0.6}Fe_{2.4}O_4$/MIL-101-NH_2 (**d**, **e**); EDS (**e**) and elemental mapping (**f**–**j**) of $Co_{0.6}Fe_{2.4}O_4$/MIL-101-NH_2

process result in a large specific surface area of $Co_{0.6}Fe_{2.4}O_4$/MIL-101-NH_2.

As displayed in Fig. 4 a, the isotherms of the three materials all show typical type II curves in the range of relative pressure (P•P_0^{-1}) 0–1.0, which is a typical feature of mesoporous materials and suggests strong adsorption advantages (Liu et al. 2023). It can be seen from the pore size distribution diagram that the pore sizes of them are mostly distributed between 2 and 10 nm (MIL-101-NH_2 and $Co_{0.6}Fe_{2.4}O_4$/MIL-101-NH_2) and 5 and 20 nm ($Co_{0.6}Fe_{2.4}O_4$), further confirming the mesoporous structure of the sample. The BET specific surface areas of MIL-101-NH_2, $Co_{0.6}Fe_{2.4}O_4$, and $Co_{0.6}Fe_{2.4}O_4$/MIL-101-NH_2 are 142.159, 44.796, and 240.485 m^2•g^{-1} respectively. The increase of specific surface area after recombination indicates that the porous structure of the composite components and the uniform dispersion of the components during the compounding process result in a large specific surface area of $Co_{0.6}Fe_{2.4}O_4$/MIL-101-NH_2.

The VSM curves of the synthesized samples and their respective parameters are depicted in Fig. 4 b and Table 1. It is discernible that the magnetic parameters, including saturation magnetization strength (M_s), remanent magnetization strength (M_r), and coercivity (H_c) of $Co_{0.6}Fe_{2.4}O_4$, decrease following its combination with MIL-101-NH_2. This decline can be attributed to the increase in non-collinear spin structures on the surface induced by the composite, along with the alteration in the distribution of magnetic cations in the surface layer of the magnetic particles due to the MOF coating (Wu et al. 2013). The VSM curve of $Co_{0.6}Fe_{2.4}O_4$/MIL-101-NH_2 exhibits noticeable hysteresis phenomena, with relatively small H_c values, and the hysteresis loops become narrower, steeper, and longer, signifying that the synthesized magnetic adsorbents all adhere to the characteristics of typical soft magnetic materials (Kim and Zhao 2022). Remarkably, after undergoing five cycles, the magnetic parameters of $Co_{0.6}Fe_{2.4}O_4$/MIL-101-NH_2 displayed only a slight decrease and remained responsive to quick removal by an applied magnetic field within a mere 30 s.

TGA is used to analyze the thermal stability of the adsorbents. Analyzing the weight loss profile of MIL-101-NH_2 in Fig. 4 c, it can be divided into five distinct stages: 30–148 °C (9.48%); 148–326 °C (16.12%); 326–520 °C (24.49%); 520–616 °C (10.41%), and 616–1000 °C (16.03%). These five stages correspond to the volatilization of adsorbed moisture and residual DMF in the material, the pyrolysis of the organic groups on the adsorbent, the decomposition of the MOF framework, and the fractional decomposition of the

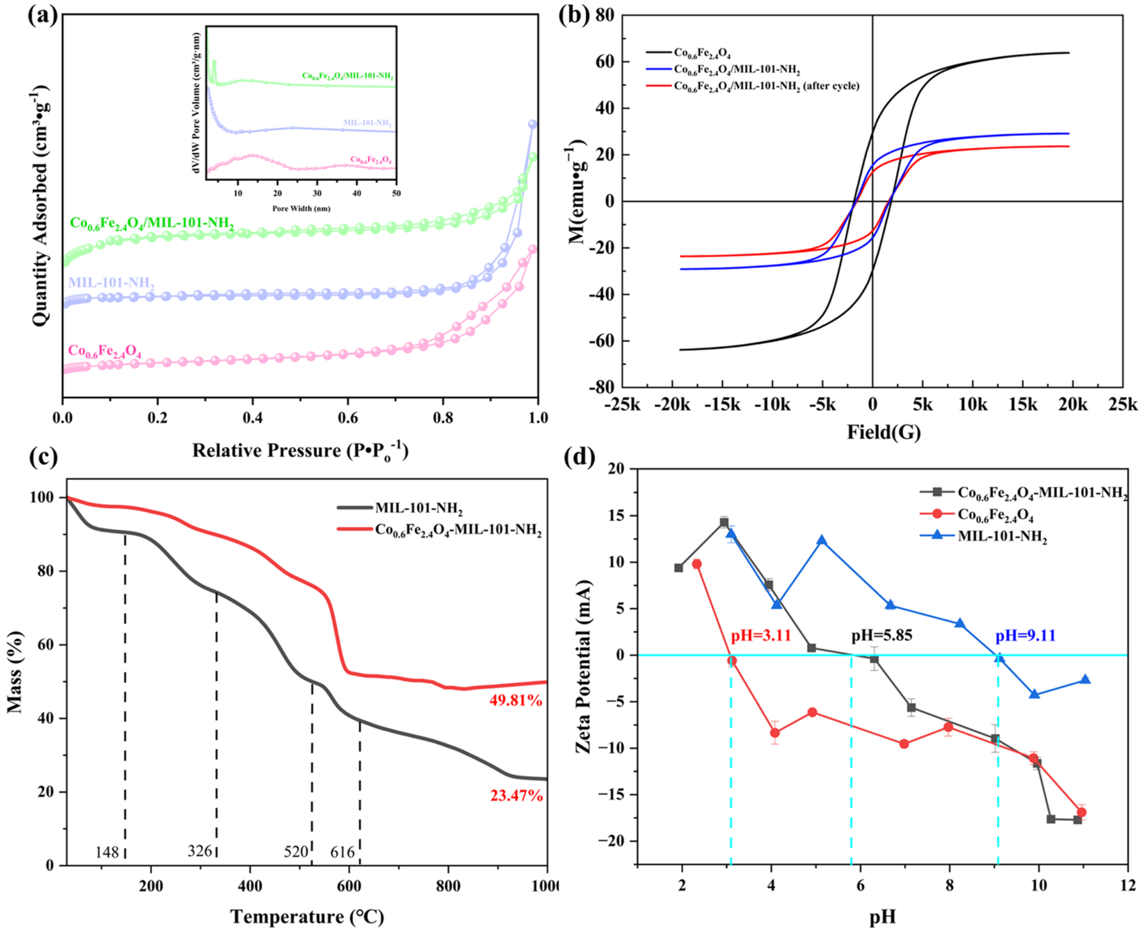

Fig. 4 Adsorption–desorption isotherms of N_2 at 77.35 K, inset: pore size distribution curve (**a**), VSM curves (**b**), TGA analysis (**c**), and zeta potential (**d**) of $Co_{0.6}Fe_{2.4}O_4$, MIL-101-NH_2, and $Co_{0.6}Fe_{2.4}O_4$/MIL-101-NH_2

Table 1 Magnetic parameters of $Co_{0.6}Fe_{2.4}O_4$, $Co_{0.6}Fe_{2.4}O_4$/MIL-101-NH_2, and $Co_{0.6}Fe_{2.4}O_4$/MIL-101-NH_2 (after five adsorption–desorption cycle) determined at room temperature

Samples	M_s (emu•g^{-1})	M_r (emu•g^{-1})	H_c (O_e)
$Co_{0.6}Fe_{2.4}O_4$	63.81	29.56	146.41
$Co_{0.6}Fe_{2.4}O_4$/MIL-101-NH_2	29.11	15.54	134.25
$Co_{0.6}Fe_{2.4}O_4$/MIL-101-NH_2 (recycle)	23.63	12.60	124.94

ligand chains, respectively (Zheng et al. 2018). $Co_{0.6}Fe_{2.4}O_4$/MIL-101-NH_2 exhibits a weight loss curve akin to MIL-101-NH_2. However, the addition of highly stable magnetic particles enhances the thermal stability of $Co_{0.6}Fe_{2.4}O_4$/MIL-101-NH_2, causing a substantially lower weight loss rate than that of MIL-101-NH_2.

The zeta potential analysis of the three materials is portrayed in Fig. 4 d. Generally, the zeta potential of the adsorbents shifts from positive to negative with increasing pH, with the point of zero charge (pH_{pzc}) measuring at 3.11 ($Co_{0.6}Fe_{2.4}O_4$), 5.85 ($Co_{0.6}Fe_{2.4}O_4$/MIL-101-NH_2), and 9.11 (MIL-101-NH_2), respectively. The inclusion of $Co_{0.6}Fe_{2.4}O_4$ significantly lowers the pH_{pzc} of MIL-101-NH_2. The zeta potential of $Co_{0.6}Fe_{2.4}O_4$/MIL-101-NH_2 shows the variation characteristics of the two component materials, which further grounds for the in-situ growth of $Co_{0.6}Fe_{2.4}O_4$ on MIL-101-NH_2.

Effect of the dosage of sorbents

To achieve adsorbent concentrations between 0.1 and 1.6 g•L^{-1}, a 50 mL solution of CR with a concentration of 100 mol•L^{-1} was treated with different dosages of the three adsorbents, ranging from 5 to 80 mg. The objective of this section is to evaluate the adsorption performance of different adsorbents and determine the ideal amount of additional adsorbent that strikes a compromise between high efficiency and affordability. Figure 5 a provides a graphic representation of the results. At an adsorbent dose of 0.1 g•L^{-1}, $Co_{0.6}Fe_{2.4}O_4$/MIL-101-NH_2 exhibited a CR removal rate of 60.10%. As the adsorbent dosage increased, the removal rate initially decreased to 47.24% before gradually ascending. The reduction in removal rate in this initial phase may be attributed to limitations in interfacial diffusion resulting from the heightened adsorbent dosage (Weber and Morris 1963). When the adsorbent dose increased from 1.2 to 1.4 g•L^{-1}, the removal rate sharply rose from 72.07 to 98.81%. However, beyond 1.6 g•L^{-1}, the removal rate experienced only marginal improvement, as adsorption approached a state of equilibrium. Consequently, considering both removal rate and economic feasibility, 0.1 g•L^{-1} was selected as the appropriate adsorbent quantity for subsequent adsorption experiments. As the adsorbent dosage rose, the equilibrium adsorption capacity of all three adsorbents generally decreased. This behavior can be explained by the fact that a significant portion of adsorption sites remain unsaturated even at equilibrium, even when the original dye concentration and volume stay unchanged. Moreover, too much adsorbent has a tendency to aggregate, which prevents dye molecules from diffusing and exposes the site, thereby partially obstructing adsorption (Tee et al. 2022). Additionally, it is worth noting that the maximum adsorption capacity of $Co_{0.6}Fe_{2.4}O_4$/MIL-101-NH_2 surpasses that of $Co_{0.6}Fe_{2.4}O_4$ and MIL-101-NH_2. However, when the adsorbent quantity exceeds 0.6 g•L^{-1}, the adsorption capacity of MIL-101-NH_2 slightly surpasses that of $Co_{0.6}Fe_{2.4}O_4$/MIL-101-NH_2. This phenomenon may be attributed to the magnetic properties of the latter, which are more prone to agglomeration and site concealment when the adsorbent quantity becomes excessive.

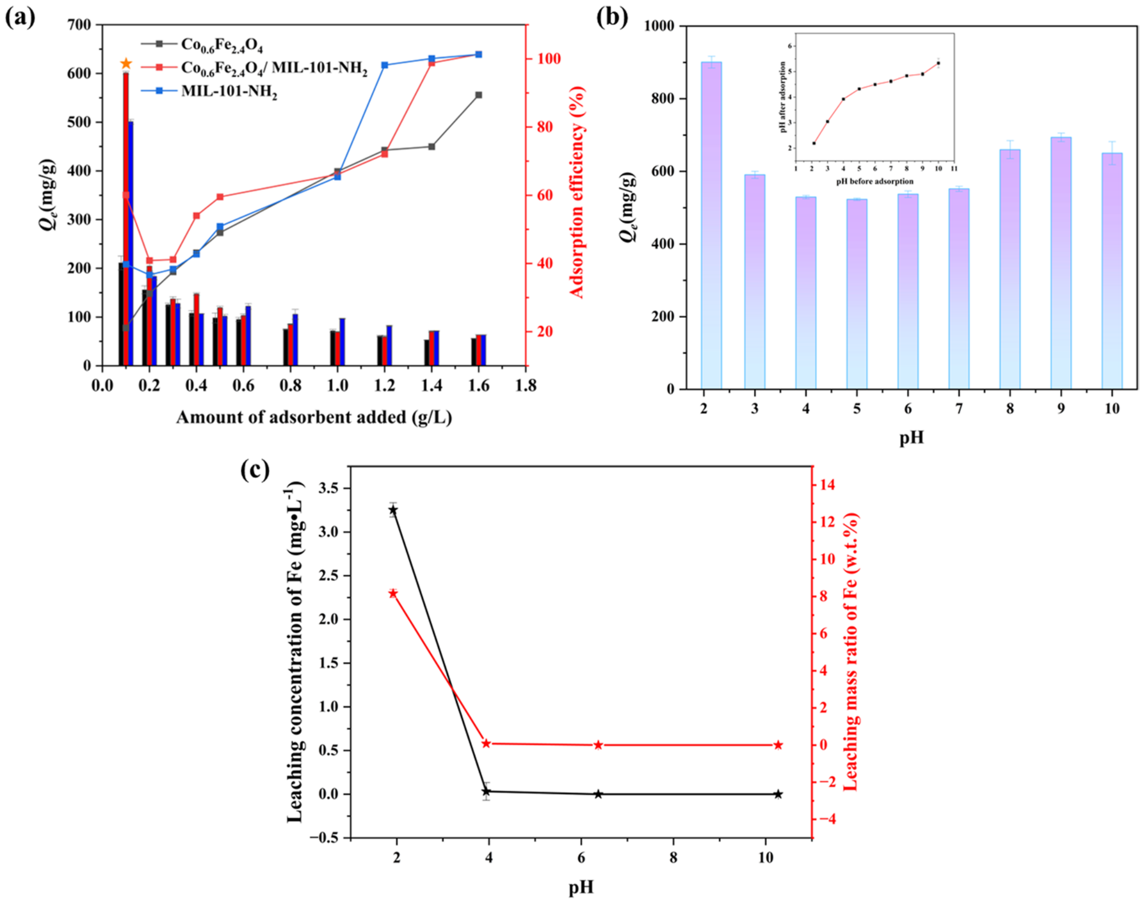

Fig. 5 Effect of adsorbent dosages (**a**) and pH (**b**) on CR removal using $Co_{0.6}Fe_{2.4}O_4$/MIL-101-NH_2 (inset: compassion of pH before and after CR adsorption; adsorption condition: 298.15 K, 24 h); **c** the leaching concentration and ratio of Fe in solution with different pH of $Co_{0.6}Fe_{2.4}O_4$/MIL-101-NH_2

Effect of pH

The pH value of dye solution determines the protonation degree of dye molecules and the charging condition of the adsorbent surface, which is one of the important factors for the adsorption behavior. Hereon the initial pH value of 2.15–10 was selected to explore the effect of pH value on the adsorption. From Fig. 5 b, when pH is 2.15, the composite adsorbent has the highest adsorption capacity for CR. Then with pH increases from 2 to 3, the adsorption capacity drops sharply. At pH is 5, the lowest adsorption capacity emerges, and followed by the overall augment of adsorption capacity with the increase of pH. The pH_{pzc} of $Co_{0.6}Fe_{2.4}O_4$/MIL-101-NH_2 is 5.85, which means that if the pH of the solution is higher than 5.85, its surface will be negatively charged; if not, it will be positively charged. The two –NH_2 and hydroxyl group (–OH) on the naphthalene ring in the CR are protonated in acidic environments, making it positively charged; in alkaline environments, the CR is present as anions as a result of their deprotonation (Csillag et al. 2023). Also the R-SO_3^- ionization from the co-color sulfonic acid groups (–SO3H) in CR is responsible for the greatest adsorption capacity under severe acidic circumstances (pH = 2.15), which permits the adsorption of CR on the positively charged $Co_{0.6}Fe_{2.4}O_4$/MIL-101-NH_2 via electrostatic attraction. Concurrently, as Fig. 5 c illustrates, 8.16% of Fe is leached from the solution in the strong acid solution (pH = 2), whereas in the weakly acidic and alkaline range, only a trace amount of Fe is leached (< 0.1%). This suggests that the leaching of iron in strong acid can liberate a portion of the adsorption site and encourage the adsorption of CR. Furthermore, The pH of all the solutions following adsorption was less than 5.33, as shown in Fig. 5 b inset. This could be attributed to the interaction between the OH– in the solution and the acid –COOH or –NH_2, which is acidic because of the presence of –SO_3H, which have a strong ability to absorb electrons on the surface of $Co_{0.6}Fe_{2.4}O_4$/MIL-101-NH_2 (Jaafar et al. 2007).

Adsorption kinetics

The pseudo-first-order kinetic model (PFO), PSO, and Elovich model (Eq. 3–5) were used to fit the correlation curve between adsorption capacity and adsorption time to evaluate the adsorption rate of the adsorbent and infer the time required to reach adsorption equilibrium. The fitting curve and related parameters are shown in Fig. 6 a–c and Table 2. For different concentrations of CR solutions, PSO has the best fitting effect, with correlation coefficients (R^2) closest to 1, which means that the adsorption process is mainly a chemical adsorption process (Hoang et al. 2019). And it is more rate limited by chemisorption, which is consistent with the previously reported adsorption behavior of MIL-101 on dye molecules. Equipped relatively fast adsorption rate, $Co_{0.6}Fe_{2.4}O_4$/MIL-101-NH_2's removal rate to CR can reach 90% in the first 12 h, and also almost attained adsorption equilibrium within 18 h. Additionally, the theoretical values of equilibrium adsorption capacity at different concentrations obtained by PSO are also closer to the experimental results, so the PSO model has high applicability. The intraparticle diffusion (ID) model (Eq. 6) was applied to analyze the diffusion process of CR molecules in the adsorbent. It is found that the adsorption process can be divided into three consecutive stages, and the fitting lines of each part do not pass the origin point (Fig. 6 d), so that ID is not the main rate-limiting step (Aly et al. 2014). The three stages are the diffusion of CR to the surface of the adsorbent, the intraparticle diffusion of CR into the inner pores of the adsorbent, and the final equilibrium stage (Xiong et al. 2021). The rate constants of the three stages show a decreasing trend, since with the increase of the adsorption time, the adsorption sites gained easy access are gradually occupied by CR molecules until the adsorption equilibrium (Wang and Wang 2008). The higher CR concentration presents to the larger rate constant of each stage.

$$Q_t = Q_{e,1}\left[1 - exp\left(-k_1 t\right)\right] \tag{3}$$

$$Q_t = \frac{k_2 Q_{e,2}^2 t}{1 + k_2 Q_{e,2} t} \tag{4}$$

$$Q_t = \beta ln\left(k_e \beta t\right) \tag{5}$$

$$Q_t = k_x \sqrt{t} \tag{6}$$

where t (min) is the adsorption time, k_1 (min^{-1}), k_2 ($g\bullet mg^{-1}\bullet min^{-1}$), k_e ($g\bullet mg^{-1}\bullet min^{-1}$), and k_x ($mg\bullet min^{-1/2}\bullet g^{-1}$) are the rate constant of PFO, PSO, Elovich, and ID kinetics, respectively; $Q_{e,1}$ and Q_{e2} are the equilibrium adsorption capacities determined by fitting of models; β($g\bullet mg^{-1}$) is the parameters related to activation energy of chemisorption.

Adsorption isotherms

Four isotherm models (Eqs. 7–10) of Langmuir, Freundlich, Temkin, and Dubinin-Radushkevich (D-R) were used to fit the results of C_e and Q_e obtained under different concentrations of CR to analyze the adsorption isotherm of $Co_{0.6}Fe_{2.4}O_4$/MIL-101-NH_2. The Fig. 7 a–d describe the non-linear fitting results of the adsorption isotherms of CR by $Co_{0.6}Fe_{2.4}O_4$/MIL-101-NH_2 at 293.15, 298.15, 303.15, and 308.15 K, and the relevant parameters are shown in Table 3. The adsorption isotherm data of CR on

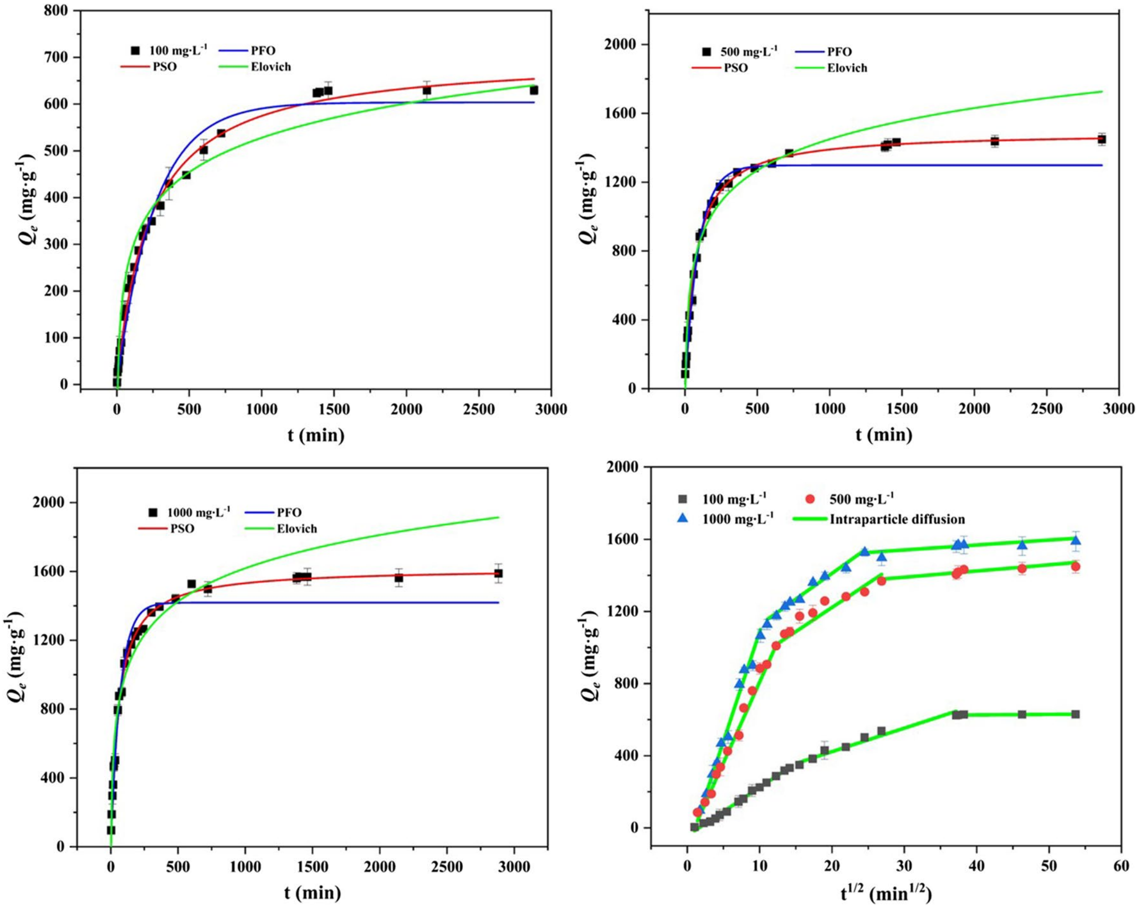

Fig. 6 The non-linearized kinetic models (PFO, PSO, and Evolich) of the adsorption of CR with different concentrations at 25 °C: **a** 100 mg•L^{-1}, **b** 500 mg•L^{-1}, and **c** 1000 mg•L^{-1}; **d** the linearized ID kinetic equation of CR adsorption with three concentrations at 25 °C

Table 2 Kinetic parameters for adsorption of CR onto $Co_{0.6}Fe_{2.4}O_4$/MIL-101-NH$_2$

Models	Parameters	Concentration		
		100 ppm	500 ppm	1000 ppm
Actual value	Q_e (mg•g^{-1})	630.03	1448.81	1588.47
PFO	$Q_{e,1}$ (mg•g^{-1})	603.70	1298.14	1418.53
	k_1 (min^{-1})	3.83E−03	1.06E−02	1.41E−02
	R^2	0.9792	0.9883	0.9818
PSO	$Q_{e,2}$ (mg•g^{-1})	705.53	1491.30	1619.00
	k_2 (g•mg^{-1}•min^{-1})	6.23E−06	9.17E−06	1.08E−05
	R^2	0.9944	0.9983	0.9985
Elovich	k_e (g•mg^{-1}•min^{-1})	1.36E−02	9.86E−04	0.011
	β (g•mg^{-1})	106.20	261.18	337.519
	R^2	0.9100	0.9616	0.9622
Intraparticle diffusion	$K_{x,1}$ (mg•min$^{-1/2}$•g^{-1})	26.74	89.49	121.44
	R^2	0.9947	0.9969	0.9918
	$k_{x,2}$ (mg•min$^{-1/2}$•g^{-1})	13.08	26.73	28.57
	R^2	0.9640	0.9739	0.9703
	$k_{x,3}$ (mg•min$^{-1/2}$•g^{-1})	0.32	3.43	2.75
	R^2	0.7118	0.7941	0.7611

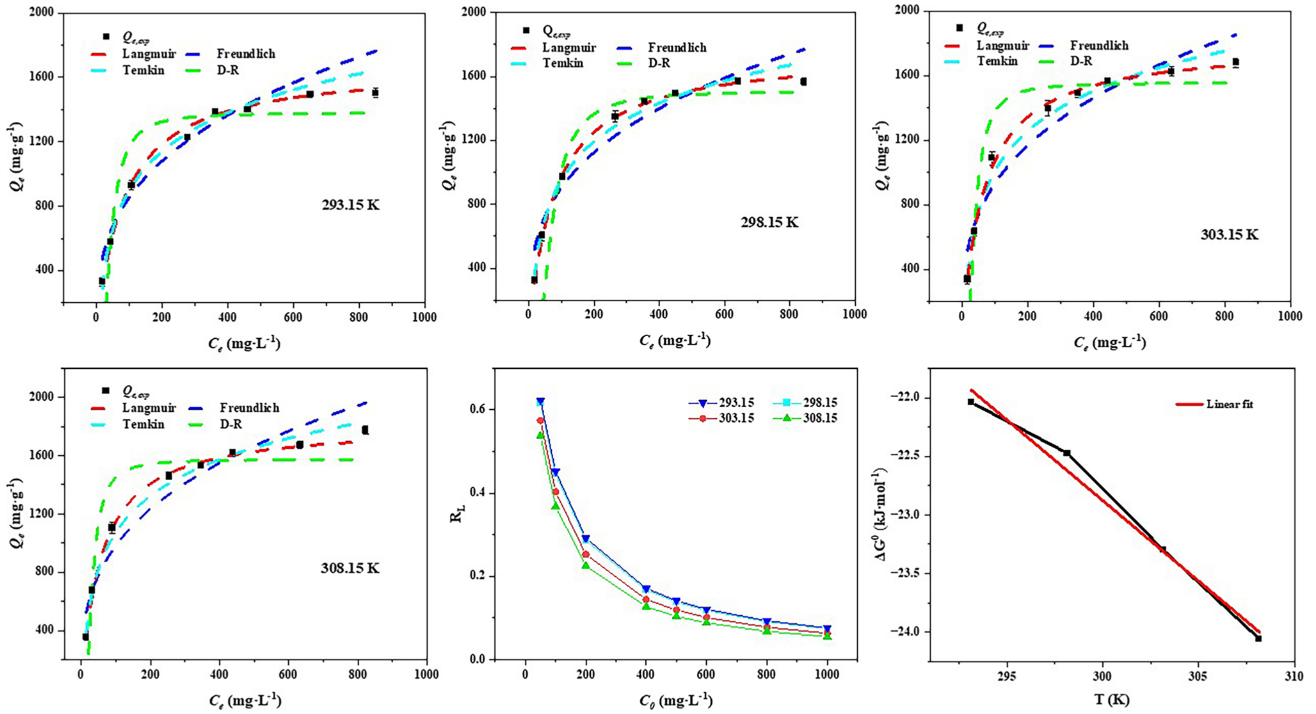

Fig. 7 Four non-linearized isotherms models (Langmuir, Freundlich, Temkin, and D-R) of the adsorption of CR at different temperatures from 293.15 to 308.15 K (**a**–**d**); the R_L values of different initial concentrations at different temperatures from 293.15 to 308.15 K (**e**); the linearized thermodynamic curve of CR adsorption on $Co_{0.6}Fe_{2.4}O_4$/MIL-101-NH_2

Table 3 Four isotherm parameters for CR adsorption on $Co_{0.6}Fe_{2.4}O_4$/MIL-101-NH_2

Models	Parameters	T (K)			
		293.15	298.15	303.15	308.15
Langmuir	$Q_{max,1}$(mg•g^{-1})	1676.48	1756.19	1797.81	1817.33
	K_L (L•mg^{-1})	1.21E−02	1.24E−02	1.48E−02	1.72E−02
	R^2	0.9924	0.9987	0.9986	0.9968
Freundlich	n	2.96	3.18	3.10	3.05
	K_F (mg•$^{(1-1/n)}$ •L$^{1/n}$•g^{-1})	180.85	213.13	211.25	217.99
	R^2	0.9461	0.9374	0.9461	0.9574
Temkin	A (L•mg^{-1})	0.13	0.16	0.17	0.33
	K_t (J•mol^{-1})	347.54	345.04	356.12	359.88
	R^2	0.9848	0.9904	0.9906	0.9953
D-R	$Q_{max,2}$(mg•g^{-1})	1380.74	1512.23	1556.58	1567.71
	K_D (mol^2•kJ $^{-2}$)	2.80E−04	6.64E−04	1.95E−04	1.27E−04
	E_a(kJ•mol^{-1})	42.27	27.44	50.69	77.43
	R^2	0.9167	0.8453	0.9188	0.9110

$Co_{0.6}Fe_{2.4}O_4$/MIL-101-NH_2 fitted well with the four isotherm equations ($R^2 = 0.85$–0.99), and among them Langmuir thanks to the highest fitting degree (R^2 is closer to 1) is more suitable for describing the adsorption equilibrium of CR on $Co_{0.6}Fe_{2.4}O_4$/MIL-101-NH_2. The isotherms' fitting results manifest that the adsorption of CR on $Co_{0.6}Fe_{2.4}O_4$/MIL-101-NH_2 is monolayer adsorption and the surface chemisorption occupied center stage (Valadi et al. 2020). Meanwhile, the maximum theoretical equilibrium adsorption capacity of $Co_{0.6}Fe_{2.4}O_4$/MIL-101-NH_2 for CR is 1756.19 mg•g^{-1} at 298.15 K, which reflects the excellent adsorption performance of $Co_{0.6}Fe_{2.4}O_4$/MIL-101-NH_2. All the R_L calculated (Eq. 11) within the range of 0–1, and the higher the CR concentration with the lower the R_L value (Fig. 7 e), i.e., the adsorption process is favorable at the four temperatures, and the easiness of adsorption increased with the increase of CR concentration. The higher temperature has the lower R_L, so the high temperature is conducive to this adsorption (Xiong et al. 2021). The E_a values obtained by the D-R model (Eq. 12) are 42.27, 27.44, 50.69, and 77.43 kJ•mol^{-1}, respectively, all exceeding 16 kJ•mol^{-1}, illustrating that the adsorption of CR on the composite is mainly chemical adsorption, which is consistent with the fitting results of the kinetic model.

$$Q_e = \frac{C_e Q_{max,1} K_L}{1 + C_e K_L} \tag{7}$$

$$Q_e = K_F C_e^{\frac{1}{n}} \tag{8}$$

$$Q_e = \frac{RT}{K_T} ln\left(AC_e\right) \tag{9}$$

$$Q_e = Q_{max,2} exp\left\{-K_D\left[RTln\left(1 + \frac{1}{C_e}\right)\right]^2\right\} \tag{10}$$

$$R_L = \frac{1}{1 + C_0 K_L} \tag{11}$$

$$E_a = \frac{1}{\sqrt{2K_D}} \tag{12}$$

where C_e (mg•L^{-1}) is the equilibrium concentration of CR solution; Q_e (mg•g^{-1}) is the equilibrium adsorption capacity; $Q_{max,1}$ and $Q_{max,2}$ (mg•g^{-1}) are the maximum adsorption capacities calculated by Langmuir and D-R model, respectively; K_L (L•mg^{-1}), K_F (mg•$^{(1-1/n)}$ •L$^{1/n}$•g^{-1}), K_T (J•mol^{-1}), and K_D (mol^2•kJ^{-2}) are the adsorption coefficients of Langmuir, Freundlich, Temkin, and D-R isotherm, respectively; n is the Freundlich constant connected with adsorption intensity; R is molar gas constant and its value is 8.314 J•mol^{-1}•K^{-1}; A (L•mg^{-1}) is adsorption equilibrium binding constant; R_L is a constant relevant to the affinity between adsorbent and adsorbate; and E_a (kJ•mol^{-1}) is free energy of adsorption.

Adsorption thermodynamics

The adsorption behavior was studied using thermodynamics, and Gibbs free energy (ΔG^0), entropy change (ΔH^0), and enthalpy change (ΔS^0) were gained through Eqs. (13)–(15) calculation and fitting. These aimed at determining the energy change, the order or disorder of the reaction, and the ability to proceed spontaneously of the adsorption process.

$$K = K_W K_L \tag{13}$$

$$\Delta G^0 = -RT\ln K \tag{14}$$

$$\Delta G^0 = \Delta H^0 - T\Delta S^0 \tag{15}$$

where K_w (mg•mol^{-1}) is the molar mass of CR.

The fitting results and the parameters are shown in Table 4 and Fig. 7 f and the equation fit better reaching $R^2 = 0.9847$. The ΔG^0 values for the adsorption CR using $Co_{0.6}Fe_{2.4}O_4$/MIL-101-NH$_2$ are – 22.04, – 22.47, – 23.30, and – 24.06 kJ•mol^{-1} at 288.15–308.15 K, respectively. All the negative ΔG^0 values manifest that the adsorption process can proceed spontaneously (Munagapati and Kim 2017; Valadi et al. 2020). The effect of the transformation of functional groups on the surface chemistry of the adsorbent at high temperature causes the ΔG^0 to decrease with increasing temperature, signifying that high temperature can promote the adsorption. The positive ΔH^0 and ΔS^0 values of $Co_{0.6}Fe_{2.4}O_4$/MIL-101-NH$_2$ manifest that the removal of CR is exothermic and that as the adsorption proceeds (Mazloomi et al. 2019). The CR and $Co_{0.6}Fe_{2.4}O_4$/MIL-101-NH$_2$ interface with an increased probability of random collisions between them may come down to the desorption of water molecules from $Co_{0.6}Fe_{2.4}O_4$/MIL-101-NH$_2$'s surface (Al Sharabati and Sabouni 2020; Gökmen and Serpen 2002). Hence, the adsorption of CR on $Co_{0.6}Fe_{2.4}O_4$/MIL-101-NH$_2$ is an endothermic, spontaneous, and orderly course (Tan et al. 2019).

Effect of co-existing ions

There are usually various anions and cations in the actual wastewater, which may have a certain effect on the adsorption of CR. The 0.1 M ionic strength for Na^+, K^+, Ca^{2+}, Mg^{2+}, Cl^-, NO_3^-, CO_3^{2-}, and SO_4^{2-} were selected for batch

Table 4 Thermodynamic parameters for CR adsorption on $Co_{0.6}Fe_{2.4}O_4$/MIL-101-NH$_2$

Temperature (K)	ΔG^0 (kJ•mol^{-1})	ΔH^0 (kJ•mol^{-1})	ΔS^0 (kJ•mol^{-1}•k^{-1})	R^2
293.15	– 22.04	18.38	0.14	0.9847
298.15	– 22.47			
303.15	– 23.30			
308.15	– 24.06			

adsorption experiments to investigate the interference of these ions. Other experimental conditions were kept consistent, and a blank group was set for control. From Fig. 8 a, the presence of Na^+ and K^+ somewhat suppressed the adsorption of CR, and the adsorption capacity decreased by 21.86% and 9.08%, respectively. Inversely, the equilibrium adsorption capacity of CR increased significantly when two divalent cations, Ca^{2+} and Mg^{2+}, were present in the solution. These probably because Ca^{2+} and Mg^{2+} could form an intramolecular bridge with the $–COO^−$ on $Co_{0.6}Fe_{2.4}O_4$/MIL-101-NH_2 for better recognizing the negatively charged CR, while the divalent cations could shield off the negative charge on the surface of the adsorbent (Vermohlen et al. 2000). The higher adsorption capacity was achieved through the enhancement of electrostatic adsorption. For the anions (Fig. 8 b), the reduction of adsorption capacity comes down to their surface competition on the sorbent. Among them, $CO_3^{2−}$ has the strongest interfering ability, probably since its greatly change to the pH of the solution and then alter the adsorption (Ding et al. 2020).

Reusability study

Eluents of 0.1 M NaOH and EtOH were used to pretreat the adsorbent, respectively. And it was discovered that the latter, when used as an eluent, had a greater regeneration effect. In contrast, 0.1 M NaOH had a larger CR elution impact, but the adsorbent sites were adversely affected by its alkalinity, which decreased the regenerated $Co_{0.6}Fe_{2.4}O_4$/MIL-101-NH_2's adsorption performance. Therefore, in order to assess the reusability of $Co_{0.6}Fe_{2.4}O_4$/MIL-101-NH_2, EtOH was used as the eluent for five adsorption–desorption cycles. Figure 8 c presents the findings. It is evident that as the number of cycles increases, the adsorption performance declines, which is brought on by the uneluted CR molecules taking up some space on the site. $Co_{0.6}Fe_{2.4}O_4$/MIL-101-NH_2 continues to have a high capacity for adsorbing CR after five cycles, and the removal rate is around 78% of the original adsorption. $Co_{0.6}Fe_{2.4}O_4$/MIL-101-NH_2 has strong cycle reusability for removing CR from water, to put it briefly.

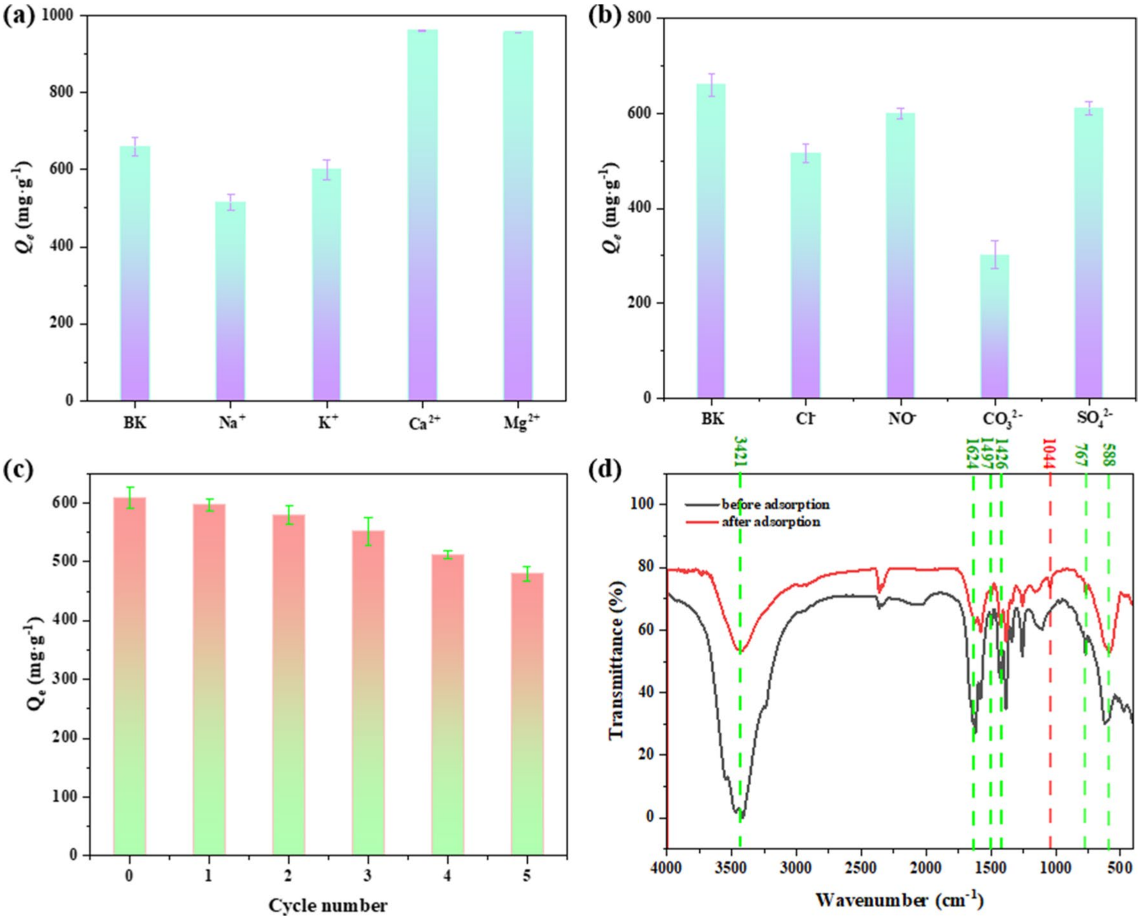

Fig. 8 Effect of different cations (**a**) and anions (**b**) on CR removal using $Co_{0.6}Fe_{2.4}O_4$/MIL-101-NH_2 at the equilibrium time; the reusability of $Co_{0.6}Fe_{2.4}O_4$/MIL-101-NH_2 for CR (**c**); the FT-IR spectra of $Co_{0.6}Fe_{2.4}O_4$/MIL-101-NH_2 before and after adsorption (**d**)

Adsorption mechanisms

In line with the electrostatic interaction theory (Gilson 1995), when the solution is barely neutral, the CR molecules can be attracted by electrostatic force to achieve the adsorption of CR because they have no charge on their surface and the positive charge for $Co_{0.6}Fe_{2.4}O_4$/MIL-101-NH_2. Even in the face of electrostatic repulsion, the adsorbent retains a high adsorption capacity for CR in strongly acidic and basic conditions, according to the results of the pH effect on adsorption. Stated differently, the adsorption process of CR on $Co_{0.6}Fe_{2.4}O_4$/MIL-101-NH_2 is a product of many processes and is impacted by mechanisms other than electrostatic interactions, such as hydrogen bonding.

The increased adsorption capacity of the adsorbent on CR under acidic and basic conditions can be explained by the –NH_2 and –OH in $Co_{0.6}Fe_{2.4}O_4$/MIL-101-NH_2 and CR serving as H-donors or acceptors to enhance adsorption through hydrogen bonding. The direction of hydrogen bonding can also be judged by the effect of pH to adsorption (Stockton and Rubner 1997). At low pH levels, if the adsorbent's –NH_2 functions as an H-donor, it is likely to get protonated, which facilitates the uptake of protons by groups like –SO_3H on CR and encourages the creation of hydrogen bonds, which in turn increases the adsorption capacity. This is consistent with the result that the adsorption capacity of CR increases with acidity so the hydrogen bonding is formed by $Co_{0.6}Fe_{2.4}O_4$/MIL-101-NH_2 as the donor and the CR molecule as the acceptor; at high pH, adsorption capacity will decrease if $Co_{0.6}Fe_{2.4}O_4$/MIL-101-NH_2's –NH_2 acts as the H-donor and readily accepts OH– in the solution; however, in alkaline conditions, adsorption performance improves, suggesting that the CR molecule is the H-donor and the adsorbent is the H-acceptor in such a scenario (Chen et al. 2022).

Figure 8 d displays the comparison of FT-IR spectra of $Co_{0.6}Fe_{2.4}O_4$/MIL-101-NH_2 before and after adsorption. A new peak at 1044 cm^{-1} corresponding to the C–N stretching vibration on CR is clearly observed after adsorption (Banerjee et al. 2016). The characteristic peaks at 585, 769, 1431, 1492, and 1617 cm^{-1} all show some shifts in the adsorption of CR. These mean that CR is adsorbed on the adsorbent. The peak of C = C changes from 1492 to 1497 cm^{-1}, which represents that there is π-π interaction between CR and adsorbent (Yuan et al. 2015). And the peak of N–H offsets from 1617 to 1624 cm^{-1}, which further confirmed the hydrogen bonding interaction between $Co_{0.6}Fe_{2.4}O_4$/MIL-101-NH_2 and CR (Kazim et al. 2020).

The adsorption mechanism of CR on $Co_{0.6}Fe_{2.4}O_4$/MIL-101-NH_2 was further verified by XPS characterization. The full spectrum before adsorption is shown in Fig. 9 a, from which the spectral peaks of five elements, C1s, O1s, N1s, Fe 2p, and Co 2p, can be clearly observed. This further supports the distribution and attachment of $Co_{0.6}Fe_{2.4}O_4$ on the surface of MIL-101-NH_2 from the side. The fine spectra of four elements, C, O, Fe, and Co, are shown in Fig. 9 b–e. Through the peak fitting of C 1 s, three peaks of 288.50, 286.50, and 284.80 eV can be obtained, which correspond to O–C = O (C1), O–C–O/C–N (C2), and C–C/C = C (C3), respectively (Wang et al. 2023). O1s is deconvolved to form C = O at 534.65 eV (COO– of MIL-101-NH_2), C–O at 531.89 eV (metal carboxylate formed by coordination of

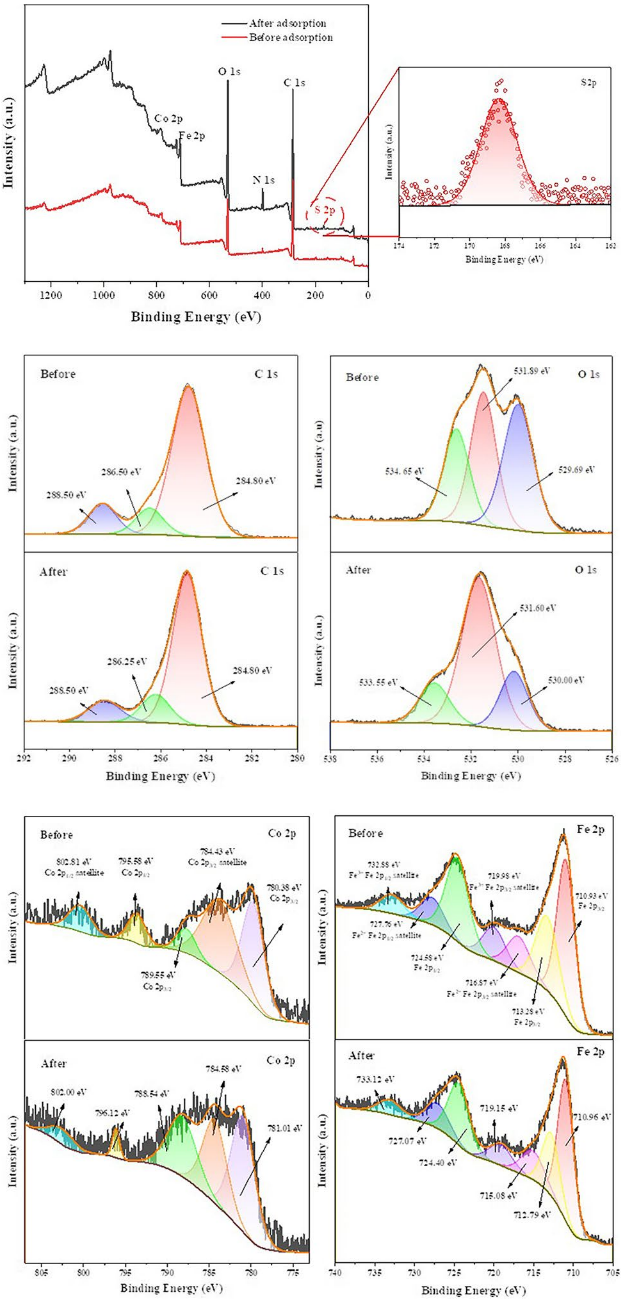

Fig. 9 XPS spectra of the $Co_{0.6}Fe_{2.4}O_4$/MIL-101-NH_2 sorbent before and after CR adsorption: **a** full-scan spectra (inset: P 2p), **b** C 1 s, **c** O 1 s, **d** Fe 2p, and **e** Co 2p

central metal Fe^{3+} of MIL-101-NH_2 with carboxylic acid ligand), and Co–O/Fe–O at 529.69 eV ($Co_{0.6}Fe_{2.4}O_4$ in the component). The double peaks and satellite peaks of Fe^{3+} and Fe^{2+} can be fitted from the deconvolution peak of Fe 2p, which manifests that Fe exists in two valence states (II and III) in $Co_{0.6}Fe_{2.4}O_4$/MIL-101-NH_2 (Biesinger et al. 2011). The peaks of Co 2p at 802.81, 795.58, 789.55, 784.43, and 780.38 eV are consistent with the XPS peak of CoO and Co_3O_4, indicating that Co exists in the form of divalent and tervalent in $Co_{0.6}Fe_{2.4}O_4$. After the adsorption of CR, the peak of S 2p appeared on the adsorbent, indicating that CR was adsorbed successfully. And it is found that the peak area ratio of C2 to C3 decreased from 0.20 to 0.14, revealing that the π-π interaction between CR and the adsorbent is weak, which is not the dominant mechanism of CR adsorption on $Co_{0.6}Fe_{2.4}O_4$/MIL-101-NH_2 (Yang et al. 2006). The decrease of the binding energy of the O 1 s peak near 531.89 eV and the increase of the peak area may manifest that some new chemical groups or surface defect sites interacting with CR have been formed on the surface of the adsorbent. The change of the binding energy of each peak in O1s indicates that some new chemical bonds or surface defect sites interacting with CR may be formed on the surface of the adsorbent, indicating that the hydrogen bond may be one of the dominant mechanisms. The peaks of Fe 2p and Co 2p shift to a certain extent after the adsorption of CR, suggesting that Fe and Co are the adsorption sites of the adsorbents. The nitrogen-containing groups on CR have the ability to establish coordination bonds with Fe and Co during the adsorption process, which will allow CR molecules to partially transfer the charge to the iron and cobalt atoms on $Co_{0.6}Fe_{2.4}O_4$/MIL-101-NH_2's surface (Lei et al. 2020). Concurrently, the adsorption process modifies the charge state of metal species, resulting in a shift in peak area. This phenomenon is associated with the emergence of interacting metal species on the $Co_{0.6}Fe_{2.4}O_4$/MIL-101-NH_2's surface. In summary, the combined effects of π-π interactions, electrostatic interactions, hydrogen bonding, and metal coordination lead to the adsorption of CR on $Co_{0.6}Fe_{2.4}O_4$/MIL-101-NH_2 (Fig. 10).

Comparison of adsorption capacity

The adsorption capacity, adsorbent dose, temperature, and adsorption equilibrium time in this work were compared with those of previously published materials for the removal of CR, as indicated in Table 5, to illustrate the superior performance of $Co_{0.6}Fe_{2.4}O_4$/MIL-101-NH_2. As can be observed, $Co_{0.6}Fe_{2.4}O_4$/MIL-101-NH_2 has a far better adsorption capacity than the majority of other publications with comparable data. $Co_{0.6}Fe_{2.4}O_4$/MIL-101-NH_2 only needs 0.1 $g•L^{-1}$ of adsorbents to successfully remove CR, whereas some documented systems can reach high adsorption capacity only by adding more adsorbents. The primary drawback of our work is the comparatively high number of preparation steps, which will partially raise the material's preparation costs. However, the benefit is that $Co_{0.6}Fe_{2.4}O_4$/MIL-101-NH_2 we created has excellent thermal stability, high recovery and reuse performance, strong selectivity, and a significant adsorption capacity for CR. Adsorbent costs can be significantly decreased. In summary, the $Co_{0.6}Fe_{2.4}O_4$/MIL-101-NH_2 developed in this work offers benefits for CR removal.

Selectivity study

MB and MO were chosen as representative cationic and anionic dyes, respectively, to probe the adsorption selectivity of $Co_{0.6}Fe_{2.4}O_4$/MIL-101-NH_2. The before-and-after UV and physical diagrams of the adsorption of $Co_{0.6}Fe_{2.4}O_4$/

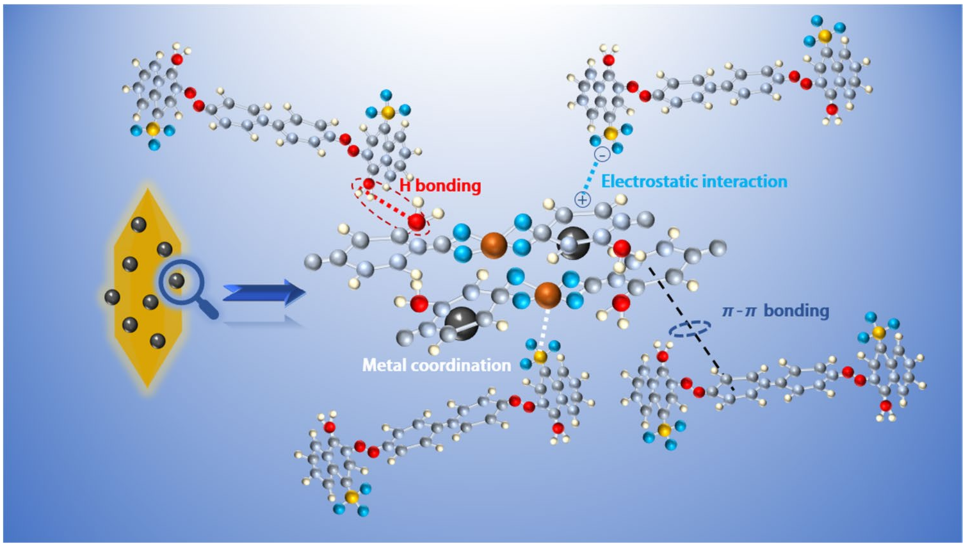

Fig. 10 The main adsorption mechanism of CR on the $Co_{0.6}Fe_{2.4}O_4$/MIL-101-NH_2

Table 5 Q_{max} of some reported adsorbents for CR

Adsorbent sample	Adsorbent dosage ($g \bullet L^{-1}$)	Temperature (K)	Adsorption capacity ($mg \bullet g^{-1}$)	Refer
La-MOF-NH_2@Fe_3O_4	0.4	298.15	716.2	Valadi et al. (2020)
$Ni_{0.6}Fe_{2.4}O_4$ nanoparticles	0.8	298.15	72.73	Zeng et al. (2014)
MIL-101(Fe)	0.1	293.15	1367.1	Zhang et al. (2020)
MIL-53(Fe)	0.1	318.15	1482	Xie et al. (2017)
CoFe-MOF	1.0	298.15	1935.68	Liu et al. (2022b)
Kaolinite supported $CoFe_2O_4$	0.1	298.15	547	Olusegun and Mohallem (2020)
Mn-UiO-66@GO-NH_2	0.1	298.15	1265.82	Eltaweil et al. (2021)
HP-β-CD/PEG400-modified Fe_3O_4 particles	1.2	303.15	1895	Yu et al. (2014)
Fe_3O_4 particles			97.62	
Co-MOF	0.1	298.15	1019.06	Guo et al. (2020)
ZIF-67			1044.58	
PEI@MDC	0.4	303.15	1723.86	Hu et al. (2022)
MOF-235	0.2	298.15	1131	Duo et al. (2019)
Co-MOF-1	0.1	293.15	1100	Zhao et al. (2022)
NH_2-MIL-101(Cr)	1.0	298.15	1206	Tan et al. (2019)
Fe_3O_4@Carbon@ZIF-8	0.6	318.15	756.88	Xiong et al. (2021)
$Co_{0.6}Fe_{2.4}O_4$/MIL-101-NH_2	0.1	298.15	1756.19	This study

MIL-101-NH_2 to the three dyes under the same conditions reveal that $Co_{0.6}Fe_{2.4}O_4$/MIL-101-NH_2 has the largest adsorption capacity for CR, followed by MO, which is also an anionic dye, and MB has the smallest adsorption capacity (Fig. 11 a–d). The better adsorption capacity of $Co_{0.6}Fe_{2.4}O_4$/MIL-101-NH_2 for the anionic dyes further indicates the contribution of electrostatic interaction in the adsorption. $Co_{0.6}Fe_{2.4}O_4$/MIL-101-NH_2 is generally good

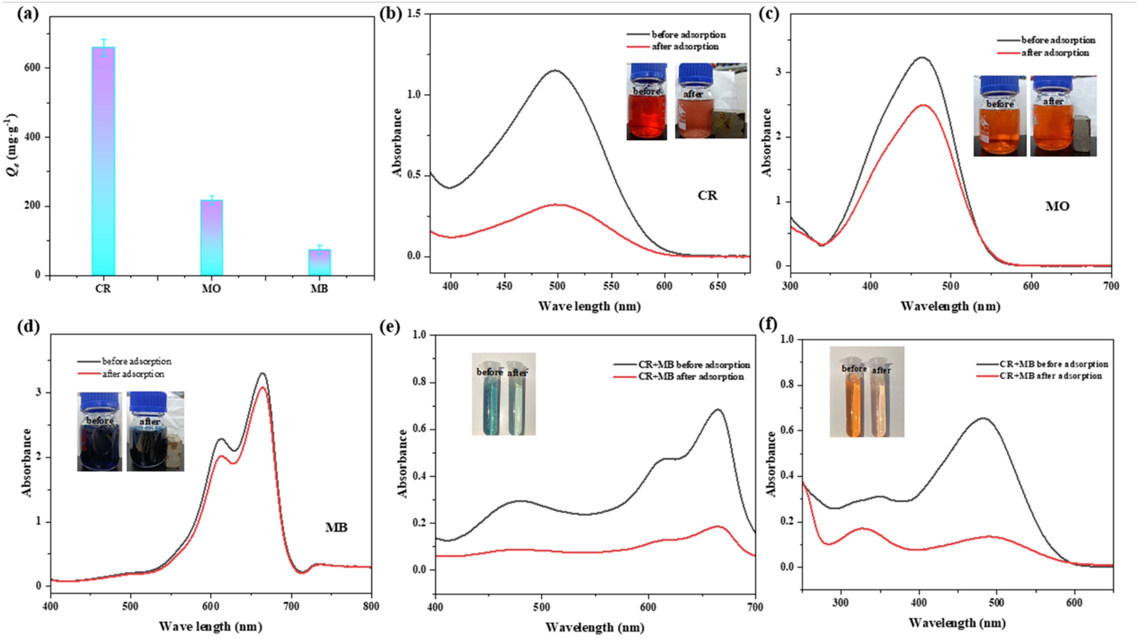

Fig. 11 **a** Comparison of adsorption capacity of $Co_{0.6}Fe_{2.4}O_4$/MIL-101-NH_2 to 100 $mg \bullet L^{-1}$ CR, 100 $mg \bullet L^{-1}$ MB, and 100 $mg \bullet L^{-1}$ MO; the ultraviolet absorption scanning spectrum actual photographs and of adsorption by $Co_{0.6}Fe_{2.4}O_4$/MIL-101-NH_2: **b** CR, **c** MO, **d** MB single solution, and **e** 50 $mg \bullet L^{-1}$ CR/10 $mg \bullet L^{-1}$ MB, **f** 50 $mg \bullet L^{-1}$ CR/50 $mg \bullet L^{-1}$ MO mixture solution

for selective adsorption of CR in the presence of competing dye molecules. In the binary mixture of dyes, the preferential adsorption of $Co_{0.6}Fe_{2.4}O_4$/MIL-101-NH_2 on CR is evident from the UV spectral peaks and the color change of the solution before and after adsorption. But the specificity adsorption capacity is relatively poor in the binary system with the same anionic dyes, probably because of the stronger competitiveness between CR and MO, resulting in the preferential occupation of some sites by MO (Xiong et al. 2021).

Conclusion

The magnetically separable adsorbent $Co_{0.6}Fe_{2.4}O_4$/MIL-101-NH_2 was synthesized and successfully applied to CR treatment. With a little amount of adsorbent (0.1 g•mL^{-1}), an ultra-high adsorption capacity (1756.19 mg•g^{-1}) can be attained. The produced adsorbent displays outstanding adsorption performance in a wide pH range (pH = 2.15–10) and high concentration (1000 mg•L^{-1}). The results of isotherm fitting and kinetics show that chemical adsorption predominates when CR is adsorbed by $Co_{0.6}Fe_{2.4}O_4$/MIL-101-NH_2, and higher temperatures promote adsorption. The adsorption process is spontaneous, endothermic, and ordered, according to thermodynamic study. Other ions, with the exception of Ca^{2+} and Mg^{2+}, will limit the adsorbent's ability to adsorb CR, and their inhibitory effect on CR removal will go as follows: $CO_3^{2-} > Na^+–Cl^- > NO_3^- > K^+ > SO_4^{2-}$. It is discovered that hydrogen bonding, metal coordination, electrostatic π-π interaction, and electrostatic interaction are all involved in the adsorption mechanism of CR on $Co_{0.6}Fe_{2.4}O_4$/MIL-101-NH_2. In CR/MB and CR/MO binary systems, $Co_{0.6}Fe_{2.4}O_4$/MIL-101-NH_2 can also readily and selectively separate CR. In addition, the adsorbent is highly cycle-reusable and retains a high adsorption capacity even after five cycles. The adsorbent is an effective and versatile adsorbent with a broad range of applications for eliminating CR dye from wastewater, as demonstrated by all of the experimental data. Finding appropriate substrates to enhance the adsorbent's mechanical capabilities could be the next topic of attention for research, given that the adsorbent's powder form restricts its processing possibilities.

Acknowledgements The authors are grateful for constructive feedback from reviewers that helped improve an earlier version of the manuscript.

Author contribution All authors contributed to the study conception and design. Conceptualization and investigation were completed by Zhenhong Zhang and Yuye Zhong. Material preparation, data collection, and analysis were performed by Zhenhong Zhang, Yuye Zhong, and Peng Sun. Review and editing were performed by Pingping Zhao, Houbin Li, and Xinghai Liu. The first draft of the manuscript was written by Zhenhong Zhang. Zhenhong Zhang and Yuye Zhong contributed equally to this work and all authors commented on previous versions of the manuscript. All authors read and approved the final manuscript.

Funding This work was supported by the National Natural Science Foundation of China (grant number: U1830127).

Data availability Data available on request from the authors. The data that support the findings of this study are available from the corresponding author, [Li Houbin], upon reasonable request.

Declarations

Ethical approval There are no ethical issues involved in this study.

Consent for publication Written informed consent for publication of this paper was obtained from the Wuhan University of Arts and Science and all authors.

Competing interests The authors declare no competing interests.

References

Abujazar MSS, Karaagac SU, Abu Amr SS, Alazaiza MYD, Bashir MJK (2022) Recent advancement in the application of hybrid coagulants in coagulation-flocculation of wastewater: a review. J Clean Prod 345:13. https://doi.org/10.1016/j.jclepro.2022.131133

Adebayo MA, Jabar JM, Amoko JS, Openiyi EO, Shodiya OO (2022) Coconut husk-raw clay-Fe composite: preparation, characteristics and mechanisms of Congo red adsorption. Sci Rep 12:12. https://doi.org/10.1038/s41598-022-18763-y

Al Sharabati M, Sabouni R (2020) Selective removal of dual dyes from aqueous solutions using a metal organic framework (MIL-53(Al)). Polyhedron 190:12. https://doi.org/10.1016/j.poly.2020.114762

Aly Z, Graulet A, Scales N, Hanley T (2014) Removal of aluminium from aqueous solutions using PAN-based adsorbents: characterisation, kinetics, equilibrium and thermodynamic studies. Environ Environ Sci Pollut r 21:3972–3986. https://doi.org/10.1007/s11356-013-2305-6

Banerjee S, Gautam RK, Gautam PK, Jaiswal A, Chattopadhyaya MC (2016) Recent trends and advancement in nanotechnology for water and wastewater treatment: nanotechnological approach for water purification. in: Advanced Research on Nanotechnology for Civil Engineering Applications, IGI Global, 208–252. https://doi.org/10.4018/978-1-5225-0344-6.ch007

Benmaamar Z, Boutoumi H, Hamitouche H, Benmaamar H, Benmaamar A, Aggoun A (2019) Simulation of adsorption kinetics of malachite green onto activated carbon. Port Electrochim Acta 37:93–104. https://doi.org/10.4152/pea.201902093

Biesinger MC, Payne BP, Grosvenor AP, Lau LWM, Gerson AR, Smart RS (2011) Resolving surface chemical states in XPS analysis of first row transition metals, oxides and hydroxides: Cr, Mn, Fe, Co and Ni. Appl Surf Sci 257:2717–2730. https://doi.org/10.1016/j.apsusc.2010.10.051

Brown JP (1981) Reduction of polymeric azo and nitro dyes by intestinal bacteria. Appl Environ Microb 41:1283–1286. https://doi.org/10.1128/AEM.41.5.1283-1286.1981

Chen D, Yu H, Pan M, Pan B (2022) Hydrogen bonding-orientated selectivity of phosphate adsorption by imine-functionalized adsorbent. Chem Eng J 433:133690. https://doi.org/10.1016/j.cej.2021.133690

Cheng L, Huang R, Cao Q, Liu N, Li P, Sun M, Qin H, Wu L (2023) Magnetic metal-organic frameworks as adsorbents for the detection of azo pigments in food matrices. Food Chem 402:134134. https://doi.org/10.1016/j.foodchem.2022.134134

Christovam EM, Franco JH, Zocolo GJ, Almeida AMF, Marcelino MY, de Oliveira DP, Zanoni MVB (2022) Stability of acid black 210 dye in tannery industry effluent in aqueous solution is limited and generates harmful subproducts. Front Environ Sci 10:13. https://doi.org/10.3389/fenvs.2022.750647

Cross SN, Fataftah M, Jonderian A, McCalla E, Blum AS (2023) Preparation and characterization of ultra-small, monodisperse $Co_xFe_{3-x}O_4$ nanoparticles. J Magn Magn Mater 567:8. https://doi.org/10.1016/j.jmmm.2022.170345

Csillag K, Emri T, Rangel DEN, Pocsi I (2023) pH-dependent effect of Congo red on the growth of Aspergillus nidulans and Aspergillus niger. Fungal Biol-UK 127:1180–1186. https://doi.org/10.1016/j.funbio.2022.05.006

Ding XX, Gutierrez L, Croue JP, Li MR, Wang LJ, Wang YR (2020) Hydroxyl and sulfate radical-based oxidation of RhB dye in UV/H_2O_2 and UV/persulfate systems: kinetics, mechanisms, and comparison. Chemosphere 253:11. https://doi.org/10.1016/j.chemosphere.2020.126655

Duo HX, Tang H, Ma JL, Lu XF, Wang LC, Liang XJ (2019) Iron-based metal-organic framework as an effective sorbent for the rapid and efficient removal of illegal dyes. New J Chem 43:15351–15358. https://doi.org/10.1039/c9nj03370j

Eltaweil AS, Elshishini HM, Ghatass ZF, Elsubruiti GM (2021) Ultra-high adsorption capacity and selective removal of Congo red over aminated graphene oxide modified Mn-doped UiO-66 MOF. Powder Technol 379:407–416. https://doi.org/10.1016/j.powtec.2020.10.084

Esrafili A, Ghambarian M, Yousefi M (2022) Electrospun zeolitic imidazolate framework-8/poly (lactic acid) nanofibers for pipette-tip micro-solid phase extraction of carbamate insecticides from environmental samples. Arab J Chem 15:10. https://doi.org/10.1016/j.arabjc.2022.104124

Ghazvini MF, Vahedi M, Nobar SN, Sabouri F (2021) Investigation of the MOF adsorbents and the gas adsorptive separation mechanisms. J Environ Chem Eng 9:10. https://doi.org/10.1016/j.jece.2020.104790

Gilson MK (1995) Theory of electrostatic interactions in macromolecules. Curr Opin Struc Biol 5:216–223. https://doi.org/10.1016/0959-440X(95)80079-4

Gökmen V, Serpen A (2002) Equilibrium and kinetic studies on the adsorption of dark colored compounds from apple juice using adsorbent resin. J Food Eng 53:221–227. https://doi.org/10.1016/s0260-8774(01)00160-1

Guo XL, Kong LJ, Ruan Y, Diao ZH, Shih KM, Su MH, Hou LA, Chen DY (2020) Green and facile synthesis of cobalt-based metal-organic frameworks for the efficient removal of Congo red from aqueous solution. J Colloid Interf Sci 578:500–509. https://doi.org/10.1016/j.jcis.2020.05.126

He QQ, Zhao HJ, Teng ZD, Wang Y, Sun WL, Guo YL, Ji XA, Hu W, Lam SS, Li M (2023) Efficient recovery of phosphate by Fe_3O_4/La-MOF: an insight of adsorption performance and mechanism from electrochemical properties. Sep Purif Technol 314:12. https://doi.org/10.1016/j.seppur.2023.123529

Hoang LP, Van HT, Nguyen LH, Mac DH, Vu TT, Ha LT, Nguyen XC (2019) Removal of Cr(VI) from aqueous solution using magnetic modified biochar derived from raw corncob. New J Chem 43:18663–18672. https://doi.org/10.1039/c9nj02661d

Hu N, Yu JZ, Hou LR, Shi CR, Li K, Hang FX, Xie CF (2022) Amine-functionalized MOF-derived carbon materials for efficient removal of Congo red dye from aqueous solutions: simulation and adsorption studies. Rsc Adv 13:1–13. https://doi.org/10.1039/d2ra06513d

Huang Q, Yang Y, Qian JJ (2023) Structure-directed growth and morphology of multifunctional metal-organic frameworks. Coord Chem Rev 484:38. https://doi.org/10.1016/j.ccr.2023.215101

Imessaoudene A, Cheikh S, Hadadi A, Hamri N, Jean-Claude B, Amrane A, Tahraoui H, Manseri A, Mouni L (2023) Adsorption performance of zeolite for the removal of Congo red dye: factorial design experiments, kinetic, and equilibrium studies. Separations 10(1):57. https://doi.org/10.3390/separations10010057

Islam M, Mostafa M (2018) Textile dyeing effluents and environment concerns-a review. J Environ Sci Nat Res 11:131–144. https://doi.org/10.3329/jesnr.v11i1-2.43380

Jaafar J, Ismail AF, Mustafa A (2007) Physicochemical study of poly(ether ether ketone) electrolyte membranes sulfonated with mixtures of fuming sulfuric acid and sulfuric acid for direct methanol fuel cell application. Mat Sci Eng A-Struct 460:475–484. https://doi.org/10.1016/j.msea.2007.02.095

Jeong C, Ansari MZ, Anwer AH, Kim SH, Nasar A, Shoeb M, Mashkoor F (2023) A review on metal-organic frameworks for the removal of hazardous environmental contaminants. Sep Purif Technol 305:40. https://doi.org/10.1016/j.seppur.2022.122416

Jiang QS, Zhao CY, Han ZL, Yang GX, Qu N, Sun LZ, Li WP, Wang MY, Cheng ZQ (2022) Amino-functionalized polyacrylonitrile/bentonite composite membranes for effective decontamination of Pb^{2+} and Congo Red. Sep Purif Technol 287:120606. https://doi.org/10.1016/j.seppur.2022.120606

Kazim M, Siegler MA, Lectka T (2020) Close Amide NH·F Hydrogen bonding interactions in 1, 8-disubstituted naphthalenes. J Org Chem 85:6195–6200. https://doi.org/10.1021/acs.joc.0c00553

Khan AH, Aziz HA, Khan NA, Hasan MA, Ahmed S, Farooqi IH, Dhingra A, Vambol V, Changani F, Yousefi M, Islam S, Mozaffari N, Mahtab MS (2022) Impact, disease outbreak and the eco-hazards associated with pharmaceutical residues: a Critical review. Int J Environ Sci Technol 19:677–688. https://doi.org/10.1007/s13762-021-03158-9

Kim Y, Zhao XH (2022) Magnetic soft materials and robots. Chem Rev 122:5317–5364. https://doi.org/10.1021/acs.chemrev.1c00481

Lee H, Kim DI, Kim Y, Jang A (2023) Efficient one-pot synthesis of magnetic MIL-100(Fe) using nitric acid without additional Fe ion addition and adsorption behavior of charged organic compounds. Chemosphere 314:7. https://doi.org/10.1016/j.chemosphere.2022.137696

Lei C, Wang C, Chen W, He M, Huang B (2020) Polyaniline@ magnetic chitosan nanomaterials for highly efficient simultaneous adsorption and in-situ chemical reduction of hexavalent chromium: Removal efficacy and mechanisms. Sci Total Environ 733:139316. https://doi.org/10.1016/j.scitotenv.2020.139316

Li X, Tjiptoputro AK, Ding J, Xue JM, Zhu Y (2017) Pd-Ce nanoparticles supported on functional Fe-MIL-101-NH_2: an efficient catalyst for selective glycerol oxidation. Catal Today 279:77–83. https://doi.org/10.1016/j.cattod.2016.03.044

Li YS, Wang YT, He LY, Meng LZ, Lu HJ, Li XL (2020) Preparation of poly(4-vinylpyridine)-functionalized magnetic Al-MOF for the removal of naproxen from aqueous solution. J Hazard Mater 383:12. https://doi.org/10.1016/j.jhazmat.2019.121144

Lian L-L, Jiang X-H, Deng Y-H, Lou D-W (2019) Adsorption of microcystin-LR in water with metal-organic framework MIL-101(Fe). J Instrum Anal 38:5. https://doi.org/10.3969/j.issn.1004-4957.2019.09.007

Lim J, Lee S, Sharma A, Seong J, Baek SB, Lah MS (2022) Ligand functionalization of defect-engineered Ni-MOF-74. Rsc Adv 12:31451–31455. https://doi.org/10.1039/d2ra06587h

Liu D, Gu W, Zhou L, Lei J, Wang L, Zhang J, Liu Y (2023) From biochar to functions: Lignin induced formation of Fe3C in carbon/Fe composites for efficient adsorption of tetracycline from wastewater. Sep Purif Technol. 304. https://doi.org/10.1016/j.seppur.2022.122217

Liu RJ, Xie YD, Cui KF, Xie J, Zhang YX, Huang YP (2022a) Adsorption behavior and adsorption mechanism of glyphosate in water by amino-MIL-101(Fe). J Phys Chem Solids 161:10. https://doi.org/10.1016/j.jpcs.2021.110403

Liu Y, Qiu GY, Liu YF, Niu YZ, Qu RJ, Ji CN, Wang Y, Zhang Y, Sun CM (2022b) Fabrication of CoFe-MOF materials by different methods and adsorption properties for Congo red. J Mol Liq 360:10. https://doi.org/10.1016/j.molliq.2022.119405

Lu FF, Dong AQ, Ding GJ, Xu K, Li JM, You LJ (2019) Magnetic porous polymer composite for high performance adsorption of acid red 18 based on melamine resin and chitosan. J Mol Liq 294:12. https://doi.org/10.1016/j.molliq.2019.111515

Lu ZH, Tian Q, Zhou DD, Chen M, Cao YW, Zhuang LY, Liu X, Yang ZH, Senosy IA (2022) Magnetic MXene based metal organic frameworks composites: synthesis, characterization and application. J Environ Chem Eng 10:10. https://doi.org/10.1016/j.jece.2022.108037

Mahmoudian MH, Azari A, Jahantigh A, Sarkhosh M, Yousefi M, Razavinasab SA, Afsharizadeh M, Shahraji FM, Pasandi AP, Zeidabadi A, Bardsiri TI, Ghasemian M (2023) Statistical modeling and optimization of dexamethasone adsorption from aqueous solution by Fe_3O_4@NH_2-MIL88B nanorods: isotherm, kinetics, and thermodynamic. Environ Res 236:16. https://doi.org/10.1016/j.envres.2023.116773

Marnani NN, Shahbazi A (2019) A novel environmental-friendly nanobiocomposite synthesis by EDTA and chitosan functionalized magnetic graphene oxide for high removal of rhodamine B: adsorption mechanism and separation property. Chemosphere 218:715–725. https://doi.org/10.1016/j.chemosphere.2018.11.109

Mazloomi S, Yousefi M, Nourmoradi H, Shams M (2019) Evaluation of phosphate removal from aqueous solution using metal organic framework; isotherm, kinetic and thermodynamic study. J Environ Health Sci Eng 17:209–218. https://doi.org/10.1007/s40201-019-00341-6

Munagapati VS, Kim DS (2017) Equilibrium isotherms, kinetics, and thermodynamics studies for congo red adsorption using calcium alginate beads impregnated with nano-goethite. Ecotox Environ Safe 141:226–234. https://doi.org/10.1016/j.ecoenv.2017.03.036

Olusegun SJ, Mohallem NDS (2020) Comparative adsorption mechanism of doxycycline and Congo red using synthesized kaolinite supported $CoFe_2O_4$ nanoparticles. Environ Pollut 260:11. https://doi.org/10.1016/j.envpol.2020.114019

Pallach R, Keupp J, Terlinden K, Frentzel-Beyme L, Kloss M, Machalica A, Kotschy J, Vasa SK, Chater PA, Sternemann C, Wharmby MT, Linser R, Schmid R, Henke S (2021) Frustrated flexibility in metal-organic frameworks. Nat Commun 12:12. https://doi.org/10.1038/s41467-021-24188-4

Razavi L, Raissi H, Hashemzadeh H, Farzad F (2022) Strategy to improve Cu-BTC metal-organic frameworks performance in removal of rhodamine B: MD and WT-MtD simulations assessment. Npj Clean Water 5:8. https://doi.org/10.1038/s41545-022-00195-w

Sarkodie B, Amesimeku J, Frimpong C, Howard EK, Feng Q, Xu ZZ (2023) Photocatalytic degradation of dyes by novel electrospun nanofibers: a review. Chemosphere 313:16. https://doi.org/10.1016/j.chemosphere.2022.137654

Selvaraj V, Karthika TS, Mansiya C, Alagar M (2021) An over review on recently developed techniques, mechanisms and intermediate involved in the advanced azo dye degradation for industrial applications. J Mol Struct 1224:15. https://doi.org/10.1016/j.molstruc.2020.129195

Shi YT, Zou YT, Khan MS, Zhang MG, Yan J, Zheng XH, Wang WQ, Xie ZG (2023) Metal-organic framework-derived photoelectrochemical sensors: structural design and biosensing technology. J Mater Chem c 11:3692–3709. https://doi.org/10.1039/d2tc05338a

Song Y, He L, Zhang S, Liu X, Chen K, Jia Q, Zhang Z, Du M (2021) Novel impedimetric sensing strategy for detecting ochratoxin A based on NH_2-MIL-101(Fe) metal-organic framework doped with cobalt phthalocyanine nanoparticles. Food Chem 351:129248. https://doi.org/10.1016/j.foodchem.2021.129248

Stockton W, Rubner M (1997) Molecular-level processing of conjugated polymers. 4. Layer-by-layer manipulation of polyaniline via hydrogen-bonding interactions. Macromolecules 30:2717–2725. https://doi.org/10.1021/ma9700486

Tan YM, Sun ZQ, Meng H, Han YD, Wu JB, Xu JL, Xu Y, Zhang X (2019) Efficient and selective removal of congo red by mesoporous amino -modified MIL-101(Cr) nanoadsorbents. Powder Technol 356:162–169. https://doi.org/10.1016/j.powtec.2019.08.017

Tee GT, Gok XY, Yong WF (2022) Adsorption of pollutants in wastewater via biosorbents, nanoparticles and magnetic biosorbents: a review. Environ Res 212:20. https://doi.org/10.1016/j.envres.2022.113248

Valadi FM, Ekramipooya A, Gholami MR (2020) Selective separation of Congo red from a mixture of anionic and cationic dyes using magnetic-MOF: experimental and DFT study. J Mol Liq 318:13. https://doi.org/10.1016/j.molliq.2020.114051

Vermohlen K, Lewandowski H, Narres HD, Schwuger MJ (2000) Adsorption of polyelectrolytes onto oxides - the influence of ionic strength, molar mass, and Ca^{2+} ions. Colloid Surface a 163:45–53. https://doi.org/10.1016/s0927-7757(99)00429-x

Wang C, Xiong C, He YL, Yang C, Li XT, Zheng JZ, Wang SX (2021a) Facile preparation of magnetic Zr-MOF for adsorption of Pb(II) and Cr(VI) from water: adsorption characteristics and mechanisms. Chem Eng J 415:11. https://doi.org/10.1016/j.cej.2021.128923

Wang HT, Yang L, Qin YH, Chen Z, Wang TL, Sun W, Wang CW (2023) Highly effective removal of methylene blue from wastewater by modified hydroxyl groups materials: adsorption performance and mechanisms. Colloid Surface a 656:12. https://doi.org/10.1016/j.colsurfa.2022.130290

Wang L, Wang AQ (2008) Adsorption properties of Congo red from aqueous solution onto surfactant-modified montmorillonite. J Hazard Mater 160:173–180. https://doi.org/10.1016/j.jhazmat.2008.02.104

Wang QZ, Zhao YJ, Shi Z, Sun XY, Bu T, Zhang CQ, Mao ZX, Li XH, Wang L (2021b) Magnetic amino-functionalized-MOF(M = Fe, Ti, Zr)@COFs with superior biocompatibility: performance and mechanism on adsorption of azo dyes in soft drinks. Chem Eng J 420:10. https://doi.org/10.1016/j.cej.2021.129955

Wang X, Ying JW, Mai YL, Zhan JJ, Chen JZ, Wen MT, Yu L (2019) MOF-derived metal oxide composite $Mn_2Co_1O_x$/CN for efficient formaldehyde oxidation at low temperature. Catal Sci Technol 9:5845–5854. https://doi.org/10.1039/c9cy01104h

Weber W, Morris J (1963) Kinetics of adsorption on carbon from solution. J SanitEng Div 89

Wu B, Lin XC, Ge L, Wu L, Xu TW (2013) A novel route for preparing highly proton conductive membrane materials with metal-organic frameworks. Chem Commun 49(143):145. https://doi.org/10.1039/c2cc37045j

Xie J, Chen W, Wu Y, Wu X, Zhao Q (2017) Highly efficient adsorption capacity of MIL-53 (Fe) metal organic framework material for Congo red. Ind Water Treatment 37:27–30

Xiong ZK, Zheng HL, Hu YD, Hu XB, Ding W, Ma JY, Li YS (2021) Selective adsorption of Congo red and Cu(II) from complex wastewater by core-shell structured magnetic carbon@zeolitic imidazolate frameworks-8 nanocomposites. Sep Purif Technol 277:18. https://doi.org/10.1016/j.seppur.2021.119053

Xu C, Yu WH, Zheng KX, Ling C, Yu ST, Jiang L (2020) Novel composite oxygen-containing resins with effective adsorption towards anilines: physical & chemical adsorption. J Chem Technol Biotechnol 95:2187–2194. https://doi.org/10.1002/jctb.6405

Yang DQ, Hennequin B, Sacher E (2006) XPS demonstration of pi-pi interaction between benzyl mercaptan and multiwalled carbon nanotubes and their use in the adhesion of Pt nanoparticles. Chem Mater 18:5033–5038. https://doi.org/10.1021/cm061256s

You LJ, Huang C, Lu FF, Wang A, Liu XC, Zhang QQ (2018) Facile synthesis of high performance porous magnetic chitosan - polyethylenimine polymer composite for Congo red removal. Int J Biol Macromol 107:1620–1628. https://doi.org/10.1016/j.ijbiomac.2017.10.025

Yu L, Xue WH, Cui L, Xing W, Cao XL, Li HY (2014) Use of hydroxypropyl-beta-cyclodextrin/polyethylene glycol 400, modified Fe_3O_4 nanoparticles for congo red removal. Int J Biol Macromol 64:233–239. https://doi.org/10.1016/j.ijbiomac.2013.12.009

Yuan Y, Shu J, Liu P, Zhang Y, Duan Y, Zhang J (2015) Study on π–π interaction in H-and J-aggregates of poly (3-hexylthiophene) nanowires by multiple techniques. J Phys Chem B 119:8446–8456. https://doi.org/10.1021/acs.jpcb.5b02805

Zeng SY, Duan SX, Tang RF, Li L, Liu CH, Sun DZ (2014) Magnetically separable Ni0.6Fe2.4O4 nanoparticles as an effective adsorbent for dye removal: synthesis and study on the kinetic and thermodynamic behaviors for dye adsorption. Chem Eng J 258:218–228. https://doi.org/10.1016/j.cej.2014.07.093

Zhang Y, Yin Y, Tong M, Sun M, Yang J (2020) Solvent synthesis of micro nano coordination polymer MIL-101 and performance research of cuperior adsorption of Congo red. Henan Chem Ind 37:18–21. https://doi.org/10.14173/j.cnki.hnhg.2020.01.005.

Zhao SQ, Chen D, Wei FH, Chen NN, Liang Z, Luo Y (2017) Removal of Congo red dye from aqueous solution with nickel-based metal-organic framework/graphene oxide composites prepared by ultrasonic wave-assisted ball milling. Ultrason Sonochem 39:845–852. https://doi.org/10.1016/j.ultsonch.2017.06.013

Zhao YZ, Zhu PZ, Pan LW, Xie YQ, Ng SW, Zhang KL (2022) Preparation and characterization of a newly constructed multifunctional Co(II)-organic framework: proton conduction and adsorption of Congo red in aqueous medium. CrystEngComm 24:3380–3393. https://doi.org/10.1039/d2ce00330a

Zheng X, Wang JL, Xue XL, Liu WX, Kong YD, Cheng R, Yuan DH (2018) Facile synthesis of Fe_3O_4@MOF-100(Fe) magnetic microspheres for the adsorption of diclofenac sodium in aqueous solution. Environ Sci Pollut Res 25:31705–31717. https://doi.org/10.1007/s11356-018-3134-4

Zheng ZJ, Xu K, Lu FF, Zhong BH, You LJ, Xiong WJ, Tang T, Wang SY (2023) Magnetic covalent organic framework for the adsorption of silver nanoparticles and recycled as surface-enhanced Raman substrate and high-efficiency catalysts for 4-nitrophenol degradation. Environ Sci Pollut Res 30:34636–34648. https://doi.org/10.1007/s11356-022-24720-z

Authors and Affiliations

Zhenhong Zhang[1] · Yuye Zhong[1] · Peng Sun[2] · Pingping Zhao[1] · Houbin Li[1] · Xinghai Liu[3]

✉ Houbin Li
lhb@whu.edu.cn

[1] School of Nursing, Wuhan University, Wuhan 430079, People's Republic of China

[2] Youyi Campus of Northwestern Polytechnical University, 127 West Youyi Road, Beilin District, Xi'an, Shaanxi 710072, People's Republic of China

[3] Electronic Information School, Wuhan University, Wuhan 430079, People's Republic of China